CHAPTER 3

APPLICATIONS FOR THE REC TECHNIQUE

In this chapter, potential applications where REC could be beneficial are explored. Specifically, three applications were evaluated where the improved axial resolution and increased bandwidth available from REC could be beneficial. First, REC was used to enhance the contrast of B-mode images using frequency compounding. Second, REC was used to improve contrast and spatial resolution of quantitative ultrasound (QUS) images.

3.1 Speckle Reduction and Contrast Resolution Enhancement of B-mode Images using REC

3.1.1 Introduction

Speckle, the granular structure in ultrasonic images, reduces the ability to detect low-contrast targets. Speckle is formed by subresolution scatterers that cause constructive and destructive interference of backscattered ultrasonic signals within the resolution cell volume of an ultrasonic source [32]. Furthermore, speckle is considered to be a deterministic process because when an object is imaged under the same operating conditions no changes in the speckle pattern occur. For these reasons, speckle is not reduced by signal averaging over time. Therefore, considerable effort has been spent over the last few decades in developing techniques to reduce speckle in ultrasonic images.

Portions of Section 3.1 have been reprinted, with permission, from J. R. Sanchez and M. L. Oelze, "An ultrasonic imaging speckle-suppression and contrast-enhancement technique by means of frequency compounding and coded excitation," *IEEE Trans. Ultrason. Ferroelect. Freq. Contr.*, vol. 56, pp. 1327-1339, Jul. 2009, ©2009 IEEE, and from J. R. Sanchez and M. L. Oelze, "An ultrasonic imaging speckle suppression and contrast enhancement technique by means of frequency compounding and coded excitation," *Proceedings of the 2007, IEEE Ultrasonics Symposium*, pp. 464-467, 2007. ©2007 IEEE.

Why speckle reduction?

In imaging, small structures or an object can be identified if the contrast between the target and the surrounding area are different [33]. Figure 3.1 shows a 1-D example of the effects that speckle can have on the detectability of low contrast targets. In ultrasonic imaging, the difference in contrast between different soft tissues can be very small. Therefore, with the use of speckle reduction techniques, image contrast can be improved by removing the interference pattern created by speckle. This intereference pattern created by speckle is also known as speckle noise and reduction of speckle noise can enhance the detectability of structures having low contrast with the background [34]. Consequently, speckle reduction techniques have been used clinically and applied to commercial systems in order to improve the detection of small structures and lesions [35].

Speckle reduction techniques

Speckle reduction techniques can be classified into two categories: post-processing techniques and compounding methods. Examples of post-processing techniques are adaptive filtering (linear and nonlinear) [36–40], deconvolution [41, 42], and wavelet despeckling [43, 44]. The compounding speckle reduction methods include spatial and frequency compounding. These schemes rely on making separate images that have uncorrelated or partially correlated speckle patterns. The separate images are then averaged to reduce the speckle while maintaining the mean intensity of the image but at the expense of spatial resolution. Originally for spatial compounding, the source aperture was translated laterally or at different angles to make images from different orientations [45, 46]. The main drawbacks of these techniques are loss in lateral resolution, and image misalignment due to motion which causes image artifacts. In addition, the need for multiple images would mean a decrease in the frame rate. Recently, manufacturers have employed receive-aperture-only spatial compounding which is not subject to frame rate losses or motion-based image registration errors because all processing is performed after the data is collected. Other advances in spatial-compounding [47, 48] use electronic beam-steering to obtain images at different angles to overcome some of these tradeoffs by using advanced image registration.

Frequency compounding

Another method, known as frequency compounding (FC), can be applied on transmit mode by using multiple sources at different frequencies or on receive mode as a post-processing speckle reduction technique by dividing the spectrum of the radio-frequency (RF) echoes into subbands to make separate and partially uncorrelated images [49–55]. The latter instance is also known as frequency diversity [50, 55], or split spectrum processing [53]. Compounding is performed by averaging the images generated from each subband. As a result of compounding, a reduction in the speckle variance is obtained while maintaining the mean intensity of the signal. As the width of the subband becomes smaller, the effective bandwidth used to create individual images decreases, which translates into a decrease in axial resolution. Therefore, the main disadvantage introduced by using frequency compounding is the inherent tradeoff between axial and contrast resolution. In fact, if a lesion is too small, loss of axial resolution may actually decrease contrast because signals from the lesion and background can smear together. Consequently, if the axial resolution and the bandwidth of an ultrasonic imaging system could be increased, these tradeoffs between axial and contrast resolution could be extended.

The first researchers that applied FC to medical ultrasound were Abbott and Thurstone [49]. In the study, they compared laser speckle to ultrasound speckle and suggested several techniques to generate independent speckle patterns including FC. Magnin et al. [51] observed that decorrelation of speckle patterns is dependent upon the excitation bandwidth and obtained increases in speckle signal-to-noise ratio (sSNR) of 26% in B-mode images using a phased array system. The sSNR is defined as the ratio of the mean to the standard deviation of the echo amplitude [32]. Melton et al. [52] developed a model to predict the amount of speckle reduction in A-mode scans based upon correlation coefficients. Trahey et al. [46] discussed a method for optimal speckle reduction based on the number of images that should be acquired within the available system bandwidth. Gehlbach et al. [50] studied frequency diversity using digital filtering techniques to determine a method to maximize sSNR and increase the ability to detect low-contrast targets. In addition, it was observed that a 10 to 15 percent increase in sSNR could be achieved by increasing the number of filters and filter overlap. Stetson et al. [56] used frequency diversity techniques with the combination of gray level mapping

to improve the contrast-to-noise ratio (CNR) of low-contrast targets. CNR assess image quality and describe the ability to perceive a target from the background region [34]. Overall, these studies suggested that FC is an effective tool for image contrast improvement. Therefore, by combining FC techniques with REC, it is hypothesized that further reductions in the variance caused by speckle could be obtained because of the larger bandwidth available.

3.1.2 Methods and procedure

The objective of using FC was to reduce the speckle noise and enhance the contrast in ultrasonic B-mode images. In the FC study, the received wideband RF spectrum was partitioned into N subbands by using Gaussian band-pass filters of smaller bandwidth than the original spectrum. These narrowband subbands were used to create separate images that had partially uncorrelated speckle patterns,i.e., up to 60% decorrelation [51]. Typically, improvements in sSNR and CNR are proportional to $\sqrt{N}$; however, because these separate images were partially correlated, the improvements should be proportional to a factor less than the square root of the sum of uncorrelated images [32]. These separate images were first normalized and then added together to reduce the speckle by reducing the image intensity variance. However, the axial resolution deteriorates because the compounded image was generated by averaging smaller subband images. The block diagram in Fig. 3.2 depicts the operation of FC for a system of N = 3. An example of FC for a system with N = 4 is shown in Fig. 3.3.

By using REC, a larger bandwidth was available, which allowed larger subbands to be used, or more importantly, an increase in the number of subbands that could be applied for a particular desired axial resolution. For this application the goal was to combine the REC technique with FC, which will be described as REC-FC, to extend the tradeoff of loss in axial resolution versus improvements in contrast. Accordingly, a parameter of interest was the bandwidth of these subbands. Therefore, in simulations and experiments, four cases were evaluated in terms of the subband width when applying FC to the REC technique. The first case consisted of using subbands that were the same width of the true impulse response bandwidth, designated as full width. The resolution of the compounded image in the full width case would be the same as that using CP

but the contrast resolution should improve due to FC. Other cases consisted of using subbands smaller than the full width, specifically, half-, third- and fourth-width of the original impulse response bandwidth. A plot showcasing the sizes of the subbands for all cases in addition to the original bandwidths of CP and REC is shown in Fig. 3.4. The cases of genuine interest are full and half width as the intention of this work was to improve the contrast without suffering a large amount of axial resolution loss. However, for study completion the later two cases, third- and fourth-width, were also evaluated. Other filter bank parameters that were considered and evaluated through simulations and experiments when applying FC to the RF spectrum were subband center frequency separation, first subband center frequency starting point, and the number of subbands. The values of these parameters were chosen so that they optimized the image quality metrics, which are defined in the following section.

Image quality metrics

To evaluate the performance of the REC-FC technique compared to CP and CP-FC the following image quality metrics were used:

1. Contrast-to-noise ratio (CNR): CNR [34], also known as contrast-to-speckle ratio, is a common quantitative measure that can assess image quality and describe the ability to perceive a target from the background region. CNR is defined as

$$CNR = \left| \frac{\mu_B - \mu_T}{\sqrt{\sigma_B + \sigma_T}} \right|, \tag{3.1}$$

where μ_B and μ_T are the mean intensity of the background and the target lesion, and σ_B^2 and σ_T^2 are the variance of the background and target, respectively. To avoid possible errors in the calculations due to attenuation, the evaluated regions of interest in the background and the target lesion were the same size and were located at the same depth.

2. Speckle signal-to-noise ratio (sSNR): sSNR [57] is a measure of the fluctuations in the speckle of a particular region of interest and is defined as

$$sSNR = \frac{\mu}{\sigma}, \tag{3.2}$$

45

where μ and σ are the mean and the standard deviation of the amplitude in the region of interest, respectively. Specifically, sSNR was evaluated for same-sized regions (900 x 20 samples, axially and laterally) in the target lesion and the background that were located at the same depth. For Rayleigh statistics, sSNR approaches 1.91 [32].

3. Histogram pixel intensity (HPI): HPI is the mean of the frequency distribution of grayscale pixel intensities and is described by

$$HPI = E\{B\}. \tag{3.3}$$

B is the histogram being evaluated and is described by

$$B(i) = c_i, \tag{3.4}$$

where c_i represents the number of pixels in the image within a particular intensity level, i, which is an integer between 0 and 255 that represents the grayscale levels used in B-mode images. Histograms were made for same-sized regions (900 x 20 samples, axially and laterally) for the target lesion and the background and located at the same depth. Ideally, for superior target detectability, there is no overlap present between the target histogram and the background histogram. Therefore, histogram overlap (HO), which is the percentage of overlapping pixels between these two regions, was also considered.

4. Lesion signal-to-noise ratio (lSNR): lSNR [57] is a ratio of contrast-detail and resolution, and therefore considers both contrast and spatial resolution for target detection. Contrast detail is an analytical measurement of image quality that quantifies the ability of the ideal observer/imaging device to detect an isolated object of minimum size at a fixed contrast, at a given level of observer confidence and for a given noise level [58]. The metric relates to the ideal observer in that it yields the dependence of lesion contrast on lesion diameter at the observer's threshold for detection [57]. The lSNR relation is defined as:

$$lSNR = \frac{C \cdot d \cdot \sqrt{N}}{\sqrt{S_{cx} \cdot S_{cz}}}, \tag{3.5}$$

where d is the diameter of the target lesion, N is the number of uncorrelated images generated with FC (N = 1 otherwise), S_{cx} and S_{cz} are the average resolution cell size in the lateral and axial direction, respectively, and C [58] is the contrast of the target and is defined by

$$C = \frac{\psi_1 - \psi_2}{\sqrt{\psi_1 + \psi_2}},\tag{3.6}$$

where ψ_1 and ψ_2 are the mean-square scattering strength (backscatter intensity) of the background and the target lesion, respectively. The average cell size is obtained using the normalized autocovariance function [59]. It is noteworthy to state that although the correlation function can be evaluated for the compounded image, the results generated are inaccurate because the uncorrelated speckle patterns are averaged, which would morph the speckle size. As a result, the average correlation function was evaluated by using one of the subband images generated. lSNR is a valuable metric in that it allows quantification of the tradeoffs between axial resolution, lesion size, and contrast between different imaging systems.

Computer simulations

Computer simulations were carried out in MATLAB (Mathworks, Natick, MA) to characterize the performance of the REC-FC technique. The simulations used a received pulse-echo pressure field model [60] described as

$$g'(x, y, t) = h_1(t) * f(x, y) * h_{pe}(y, t),\tag{3.7}$$

where x represents the axial spatial coordinate, y represents the lateral spatial coordinate, $h_1(t)$ is the pulse-echo impulse response of the transducer, $f(x, y)$ is the scattering function, and $h_{pe}(y, t)$ is the modified pulse-echo spatial impulse response that takes into consideration the geometry of the transducer and the spatial extent of the scattered field (beam diffraction). The pulse-echo impulse response, $h_1(t)$, for CP was generated by gating a sinusoid of four cycles with a Hanning window

$$w(n) = \begin{cases} 0.5 \cdot (1 - cos(\frac{2\pi n}{L_H - 1})), & 0 \le n \le L_H - 1 \\ 0, & \text{otherwise}, \end{cases}\tag{3.8}$$

47

where n is an integer and L_H is the number of samples in the window. The window and sinusoid parameters where chosen such that they matched the transducer used in experiments. As a result, the generated pulse-echo impulse response was located at the focus of a 2.25 MHz single-element transducer (f/2.66) with a fractional bandwidth of 50% at -3 dB, which would correspond to a window length of N = 128. For REC, the desired impulse response function, $h_2(t)$, was constructed to have double the fractional bandwidth, or 100% at -3 dB, compared to the CP method. Therefore, a Hanning window of half the length, N = 64, was used to construct the REC impulse response. The spatial response for a circular focused piston source can be approximated as a circular Gaussian beam [61] which is defined as

$$ h_{pe}(y,t) = \delta(t - \frac{2R_d}{c})e^{\frac{-y^2}{\sigma_y^2}}, \tag{3.9} $$

where R_d is the distance from the source to target in space, c is the speed of sound of the medium and σ_y, which was set to be equal to 1.28 mm, is the nominal lateral beamwidth of the source at -6 dB, which is the full width at half maximum.

The object being imaged was a simulated phantom that was 20 mm in length, 30 mm in width and 1.92 mm in height. The received RF backscatter data were sampled at a rate of 100 MHz. The transducer was translated laterally across the surface of the phantom in increments of 0.1 mm. A cylindrical target with a radius of 7.5 mm was located at the center of the phantom. To generate a hyperechoic target with a contrast of approximately +6 dB, the amplitude of the scattering strength from scatterers in the target lesion region was twice the amplitude of the scattering strength from scatterers in the background. To achieve fully developed speckle, the phantom contained an average of 20 point scatterers per resolution cell volume. In this dissertation, a resolution cell volume for a circular transducer is defined as a pulse length times the area of a cylinder, where the cylinder width is the lateral beamwidth. The scatterers were uniformly distributed throughout the phantom and spatially at random.

A total of 50 phantoms were simulated and evaluated with the image quality metrics discussed in Section 3.1.2. Attenuation and noise were not modeled in the simulations in order to examine the relationship of FC to the speckle reduction only. In simulations, no optimization of the γ parameter in the Wiener filter (Eq. (1.2)) was used. However,

in this study the γ parameter (Eq. (1.2)) was set to unity and then slightly adjusted until it forced the Wiener filter towards an inverse filter in order to increase the axial resolution.

Experimental setup

Experiments were performed to validate the simulations. A single-element, weakly focused (f/2.66) transducer (Panametrics, Waltham, MA) with a nominal center frequency of 2.25 MHz and a 50% (at -3 dB) fractional bandwidth (measured) was used to image a phantom by translating the transducer laterally across the phantom. There were two different experimental setups utilized: one for CP methods and another one for REC experiments. These setups would contain different noise levels due to the use of different excitation systems. Therefore, to avoid errors in the comparisons, the noise levels were normalized to an eSNR of 28 dB. Normalization of eSNR was accomplished by adding zero-mean Gaussian white noise to the CP RF echo waveform. The two experimental setups are described as follows:

1. Conventional pulsing experimental setup: The transducer was excited by a pulser-receiver (Panametrics 5800, Waltham, MA) and the receive waveform was displayed on an oscilloscope (Lecroy 9354 TM, Chester Ridge, NY) for visual verification. The echo signal was recorded at a rate of 100 MHz by a 12-bit A/D (Strategic Test Digitizing Board UF3025, Cambridge, MA) for further processing by a PC. A diagram of the experimental setup for CP is shown in Fig. 3.5(a).

2. REC experimental setup: The pre-enhanced chirp was generated in MATLAB (The Mathworks Inc., Natick, MA) and downloaded to an arbitrary waveform generator (Tabor Electronics W1281A, Tel Hanan, Israel). The excitation signal was sampled at a rate of 100 MHz and amplified by an RF power amplifier (ENI 3251, Rochester, NY). The amplified signal (50 dB) was connected to the transducer through a diplexer (Ritec RDX-6, Warwick, RI). The echo signal was received by a pulser-receiver (Panametrics 5800, Waltham, MA), which was displayed on an oscilloscope (Lecroy 9354 TM, Chester Ridge, NY) for visual verification. The echo signal was recorded at a rate of 100 MHz by a 12-bit A/D (Strategic Test

Digitizing Board UF3025, Cambridge, MA) for further processing by a PC.

A tissue-mimicking phantom (ATS Laboratories Model 539, Bridgeport, CT) and a hydrogel cone phantom were used to assess the performance of REC-FC with the image quality metrics described in Section 3.1.2. The material from the ATS tissue-mimicking phantom consisted of urethane rubber with a speed of sound of 1450 m/s $\pm$ 1.0% at 23 °C and an attenuation coefficient of 0.5 dB MHz^{-1} cm^{-1} $\pm$ 5.0%. A 15 mm diameter echogenic grayscale target structure with a constrast of +6 dB located at a depth of 4 cm into the phantom was imaged and the four FC cases were applied. Therefore, the goal of imaging with the ATS phantom was to evaluate and quantify the contrast improvements versus changes in spatial resolution for lesions of the same size but with different contrasts.

A hydrogel cone phantom was designed and fabricated at the Ultrasonic Imaging Laboratory at the Beckman Institute at the University of Illinois at Urbana-Champaign. The phantom contained a cone inclusion with a 15 mm diameter at the top. By imaging cross-sectional planes of the cone at different heights of the cone, lesions of different sizes could be imaged and evaluated. The materials (and relative amounts by weight) for the cone inclusion were type-A gelatin (Fisher Scientific, Pittsburgh, PA) (5.5%), n-propanol (9.0%), distilled and deionized water (83.4%), formaldehyde (0.1%), and powdered graphite (2.0%). The materials (and relative amounts by weight) for the surrounding medium around the cone were type-A gelatin (5.5%), n-propanol (9.0%), distilled and deionized water (84.8%), formaldehyde (0.1%), and powdered graphite (0.5%). The powdered graphite scatterers were positioned at random locations throughout the phantom by rotating the phantom before the gel congealed. In addition, the concentration difference of the powdered graphite between the cone lesion and the background provided cone-to-background contrast of +6 dB. The speed of sound and the attenuation coefficient slope of the phantom were measured to be approximately equal to 1540 m/s and 0.49 dB MHz^{-1} cm^{-1}, respectively, when using a 2.25 MHz source. The goal of imaging with the hydrogel cone phantom was to evaluate and quantify the contrast improvements by varying the size of the lesion while maintaining the same lesion-to-background contrast.

All measurements of phantoms were conducted at room temperature (approx. 23 °C) in a tank of degassed water. Furthermore, in experimental measurements, no optimization of the γ parameter in the Wiener filter (1.2) was used. Moreover, the same technique to determine the γ as described in Section 3.1.2 was used for the experimental measurements.

3.1.3 Results

Computer simulations

Descriptions of the filter banks designed for the computer simulations are given in Table 3.1. The resulting axial and lateral resolutions are given in Table 3.2. The axial resolution should deteriorate as the subband width decreases. Moreover, the values obtained for CNR and sSNR for all four cases (full-, half-, third-, and fourth-width) in addition to the reference scans (CP and REC with no compounding) are listed in Table 3.3. The values for HPI, HO, and lSNR are summarized in Table 3.4. From Table 3.3 it can be observed that both CNR and sSNR improved as the number of subbands increased and the subband width became smaller. These improvements in terms of CNR, $sSNR_B$, and $sSNR_T$ are also illustrated in Fig. 3.6(a,b,c). These graphs indicate that as the number of subbands increased the contrast as quantified by these metrics also increased.

The B-mode images representing the results are displayed in Fig. 3.7. Examination of the reference scans in Figs. 3.7(a) reveals that by using the REC technique without any compounding the speckle size was finer than when compared to CP. The smaller speckle size (i.e., better spatial resolution) resulted in the object boundaries being more well-defined because there was more detail compared to CP images. The spatial resolution boost was then traded away to improve contrast resolution by applying FC with subbands that had the same bandwidth as CP (full width) as shown in Fig. 3.7(b). For the full-width case, the CNR, $sSNR_B$, and $sSNR_T$ improved by 71%, 53%, and 51% over CP. Essentially, a gain of CNR and sSNR was achieved while maintaining the same spatial resolution that would be obtained by using CP methods. Through examination of Fig. 3.6(d), the lSNR values were higher for REC than for CP. Therefore, the increasing

51

lSNR suggests that the target detectability was increased with REC-FC compared to CP. The lSNR for REC without compounding was 15% better than that for CP without compounding. This implies that the same lSNR value would be obtained for both CP and REC, if a target of approximately 13 mm in diameter was imaged with REC compared to 15 mm imaged using CP. In other words, according to the lSNR metric, a smaller lesion would be more detectable with REC than with CP because of the spatial resolution boost.

In addition to improvements in contrast, the boundaries of the target were more defined with REC-FC when compared to CP. This edge enhancement was due to the resolution enhancement in the REC reference image which led to increased detail as shown in Fig. 3.8b. The images in Fig. 3.8 were generated by applying a -6 dB threshold on the envelopes of CP, REC, and REC-FC (full width) and then estimating the margin strength [62]. The difference in contrast between the background and the target was 6 dB; therefore, a threshold of -6 dB was considered. A threshold was applied to segment the target from the background, i.e., pixel values greater than -6 dB were considered part of the target and were assigned a value of one while all other pixel values were assigned a value of zero. Margin strength was then estimated to detect the strength of the distinct boundaries generated by applying the -6 dB threshold. Margin strength [62] is defined by the following equation:

$$MS = E\left\{\sqrt{\left(\frac{dROI}{dx}\right)^2 + \left(\frac{dROI}{dy}\right)^2}\right\}, \tag{3.10}$$

where ROI is a two-dimensional region-of-interest within the envelope. From images of the margin strength, shown in Fig. 3.8, the targets' edges were more clearly defined and outlined for REC-FC when compared to CP. For REC this was not the case. However, when carefully examining REC versus CP, it was evident that REC had less background content around the target edges when compared to CP, allowing the boundaries to be traced.

The other cases evaluated were half-, third-, and fourth-width of CP impulse response, which would translate into a reduction by a factor of two, three and four in terms of axial resolution, respectively. The half-, third-, and fourth-width case FC filter banks were applied to both CP and REC as shown in Fig. 3.7(c-e). In simulations it

was observed that the lSNR values decreased with smaller subbands in the FC. Therefore, the decreasing lSNR values suggest that the corresponding loss in axial resolution outweighed the increase in contrast obtained. In the REC-FC simulations, the lSNR for the fourth-width case suffered a significant drop, which was attributed to the deterioration of axial resolution. However, REC-FC was still better than CP-FC in terms of lSNR. A slight decrease in lSNR of 2% was encountered when comparing CP to REC-FC (fourth-width). In terms of lSNR, the improvements obtained up to the third-width case quantified significant benefits of REC-FC over CP and CP-FC.

Histograms of the background and target regions for all four cases are shown in Fig. 3.9. From examination of the reference scans in Fig. 3.9(a), a large overlap in the distribution of grayscale pixel intensities between the background and the target existed. The overlap was due to the large spread in the standard deviation about the mean pixel value of these regions. In fact, the overlap of these regions for the CP and REC reference scans was 28%. A large overlap between these two regions was undesirable because it would decrease the ability to detect the target against the background. By using FC, the overlap was reduced to 18% for the full width case as shown in Fig. 3.9(b). This decrease in overlap can be attributed to a reduction of 11.6 and 11.7 in the standard deviation of pixel intensities about the mean for the background and the target regions, respectively. Moreover, as expected (Figs. 3.9(c-e)), the percent overlap for the half-, third-, and fourth-width for CP-FC cases decreased. However, the overlap obtained with CP-FC was higher than than with REC-FC.

Experimental results: ATS phantom +6 dB contrast lesion

Descriptions of the filter banks designed for the experimental implementation are given in Table 3.5. The filter banks deviated slightly from the values obtained for the computer simulation as the bandwidth of the source was slightly different. The resulting axial and lateral resolutions are given in Table 3.6. Again, as the subband width became smaller, a decrease in axial resolution was observed. Moreover, values of CNR and sSNR obtained for all four cases (full-, half-, third-, and fourth-width) in addition to the reference scans (CP and REC with no compounding) are provided in Table 3.7. Values for HPI, HO, and lSNR are summarized in Table 3.8. A trend similar to that observed in simulations

was observed in experiments in that the CNR and sSNR improved as the subband width became smaller. Furthermore, the improvements in terms of CNR, $sSNR_B$, and $sSNR_T$ are shown in Fig. 3.6(a,b,c). The B-mode images representing these results are displayed in Fig. 3.10.

Examination of the reference scans in Fig. 3.10(a) revealed that by using the REC technique the speckle size was finer when compared to CP, which was also evident in the simulations. Next, FC was applied with subbands corresponding to the bandwidth of the original impulse response of the source under CP methods (full width) to improve contrast as shown in Fig. 3.10(b). For the full width case, the CNR, $sSNR_B$, and $sSNR_T$ using REC-FC improved by 121%, 41%, and 57% over CP. Increases in CNR and sSNR were obtained while maintaining the same axial resolution that would be obtained by using CP methods. Similar to the simulations, the definition of object boundaries was enhanced in the experimental results because the REC B-mode image contained more detail when compared to CP. Therefore, when applying REC-FC this extra information could enhance the image boundaries obtained when compared to CP. Evaluating lSNR results shown in Fig. 3.6 suggests that by using REC the lSNR improved by 48% over CP, indicating improved target detectability. This would imply that the same lSNR value would be obtained for both CP and REC if a target of approximately 7.8 mm in diameter was imaged with REC rather than 15 mm as in CP. Use of the REC technique on an ultrasound imaging system significantly improved the detectability of small targets.

A comparison of experimental results with simulations revealed the improvement for the full width case in terms of $sSNR_B$ and $sSNR_T$ remained approximately the same, while the improvement in terms of CNR was larger in the experiment (121%) than in simulations (71%). The next case evaluated was half-width of CP impulse response. The half-width case was applied to both CP and REC as shown in Fig. 3.10(c). In comparing experimental results to simulations it was observed that the improvements for the half-width case in terms of $sSNR_B$ and $sSNR_T$ were quite similar, while the improvement in terms of CNR were larger in the experiment (231%) than in simulations (137%). There were two other cases evaluated, shown in Figs. 3.10(d) and 3.10(e). For the third- and fourth-width REC-FC cases, the lSNR dropped, but maintained higher values than

CP, with increases of 139% and 130%, respectively. This decrease was related to the visible effects of target edge blurring due to the resolution decrease in B-mode images. Although the lesion is still detectible for the third- and fourth-width REC-FC cases, it is not recommended to drive REC-FC beyond the half-width case if the best performance criteria for detecting a lesion is desired. This performance criteria is associated to the decision theoretic lSNR [57].

Histograms of the background and target regions for all four cases are shown in Fig. 3.11. Examination of the reference scans shown in Fig. 3.11(a) revealed that there was a large overlap in the distribution of grayscale pixel intensities between the background and the target. This overlap was due to the large spread in the standard deviation about the mean pixel intensity of these regions. In fact, the overlap of both these regions for the CP and REC reference scans was 35%. By using REC-FC, the overlap was reduced to 33% for the full width case as shown in Fig. 3.11(b). A 2% drop is significant in that it was achieved with no cost in axial resolution because the axial resolutions for CP and REC were the same. A major difference between simulations and experiments was that the mean pixel intensity value for the background region increased during simulations while the value decreased for experimental measurements. The mean pixel intensity values for the target increased for both simulation results and experimental measurements. This change in the mean pixel value may help explain how the CNR results improved drastically during experiments compared to simulations. Another factor that may have led to the greater improvement in CNR for experimental measurements versus simulations was the fact that the simulations did not contain noise. In using a coding technique and FC, noise may be further reduced leading to enhanced CNR over just the compounding effect alone. Furthermore, the overlap for the half-, third-, and fourth-width for CP-FC cases (Fig 3.11(c,d,e)) decreased; however, the overlap obtained with CP-FC was higher when compared to REC-FC. Moreover, the simulations only considered the position of the scatterers laterally. In other words, the amplitude did not vary throughout the axial extent of the image. Consquently, the mean of the pixels in the background did not drop because the amplitude was relatively constant. Nonetheless, it should be noted that although the overlap in pixel intensities between these two regions was reduced, the reduction in axial resolution was deteriorat-

ing image quality for the third- and fourth-width cases. This reduction in image quality could reduce the ability to detect small targets. This effect was not as noticeable in the simulation results except for the fourth-width case.

Experimental results: hyrdrogel phantom with lesions of different sizes

The B-mode images obtained for the hydrogel cone phantom for various target lesion diameters are displayed as follows: 8 mm in Fig. 3.12, 5 mm in Fig. 3.13, and 3 mm in Fig. 3.14. The values of CNR, $sSNR_T$ and $sSNR_B$ for the hydrogel phantom for various lesion sizes and using various FC cases are shown in Tables 3.9, 3.10, and 3.11. The filter banks applied in this particular study were consistent with the parameters shown in Table 3.5.

The results for the 5 mm and 3 mm diameter cases can be characterized by large variability in the CNR and sSNR values. The variability in the results occurred because the regions of interest used to obtain the statistical measures of CNR and equivalently sSNR became smaller as the lesion diameter became smaller. Evaluation of the statistical measures in smaller regions of interest when using FC was problematic because of the widening of the speckle patterns as the subband widths became smaller. A MATLAB simulation was performed to evaluate the relationship between the number of pixels used in the calculation of CNR and the variance of the CNR estimates. The simulation consisted of a phantom with two regions: one representing the background and one the lesion as shown in Fig. 3.15(a). A total of 25 phantoms were imaged using CP methods and the properties of the background and lesion regions were represented by the parameters of the experimental study (i.e., the contrast between them was +6 dB). From the simulations it was estimated that around 10,000 pixels were needed to obtain a CNR with a standard deviation of 0.10 as shown in Fig. 3.15(b). The regions of interest contained 15,000, 4000, and 2250 pixels for the 8 mm, 5 mm, and 3 mm cases, respectively. The results in Fig. 3.15(b) suggests that the sample sizes were too small to obtain a precise estimate of the statistical estimates of CNR and sSNR for the 5 mm and 3 mm cases. Similar conclusions can be established regarding the sample size for the lSNR metric as it is heavily dependent on contrast. Therefore, values listed for the CNR and lSNR for the smaller lesion sizes are not as reliable as those listed for larger

lesions where more samples are available.

Combination of REC-FC images: Enhanced REC-FC

Although improvements in contrast are obtained, a detriment of REC-FC is that the smaller the subband width the more the axial resolution is degraded. As a result, the REC-FC images appeared blurry as the subband width became smaller. A method was proposed that could provide the improvements in contrast obtained with REC-FC without sacrificing as much axial resolution. The proposed method was to sum a collection of compounded images constructed from different subband widths. For the purpose of this document, this study shall be known as enhanced REC-FC, or eREC-FC. In this study, eREC-FC utilized the sum of the following images: REC reference image, REC-FC (full width), REC-FC (half width), REC-FC (third-width), REC-FC (fourth-width), and REC-FC (eighth-width) to form an enhanced final REC-FC image. Theoretically, by summing all the compounded images along with the reference, the final enhanced image hawould have an axial resolution that appeared similar to the full width or equivalently the original resolution obtained with CP. The results of summing the envelope of the reference and subbands is shown in Fig. 3.16. Evaluation of the pulse-width of the eREC-FC envelope at -10 dB in Fig. 3.16 indicated that the axial resolution was slightly better than the REC-FC full width case and the CP reference but worse than the REC reference.

The B-mode images for the various ATS phantom targets when applying eREC-FC are displayed as follows: +6 dB in Fig. 3.17, +3 dB in Fig. 3.18, -3 dB in Fig. 3.19, and -6 dB in Fig. 3.20. The CNR results obtained with eREC-FC are listed in Table 3.12. Examination of the eREC-FC and the reference B-mode images in Fig. 3.17-3.20 suggests that the spatial resolutions of the two images were quite similar; however, the eREC-FC image had improved image contrast (CNR) by an average of 133%. The CNR results obtained with eREC-FC were similar to the results obtained for the REC-FC third-width case regardless of the reference CNR value. These results were expected because averaging the images obtained for the full-, half-, third-, fourth-, and eight-width along with reference would provide a middle point between the third and fourth-width cases.

The B-mode images for the various hydrogel targets when applying eREC-FC are

displayed as follows: 8 mm in Fig. 3.21, 5 mm in Fig. 3.22, and 3 mm in Fig. 3.23. The CNR results obtained with eREC-FC are also listed in Table 3.12. Examination of the eREC-FC and the reference B-mode images in Figs. 3.21- 3.23 also suggested that the spatial resolutions of the two images were quite similar; however, the eREC-FC image had improved image contrast (CNR) by an average of 132%. The CNR for the hydrogel cone phantom obtained with eREC-FC were similar to the results obtained for the REC-FC third-width case regardless of the diameter of the lesion.

Therefore, with eREC-FC the B-mode images were drastically improved by increasing the CNR, which was between the CNR values estimated for the third-width and fourth-width REC-FC cases. Furthermore, these contrast improvements were achieved without sacrificing the axial resolution by a significant amount, which would occur under normal FC procedures.

3.1.4 Conclusion

A pulse compression and coded excitation technique, REC, was used to double the axial resolution, which translated into an increase in system bandwidth. The speckle reduction technique known as FC utilized this larger available bandwidth to improve image contrast in ultrasonic B-mode images. FC partitions the useable bandwidth by using subbands that are smaller than the system bandwidth to improve image contrast and reduce speckle noise but at the expense of axial resolution. Therefore, the major objective of this study was to establish the benefits of applying FC to REC to take advantage of the larger useable bandwidth to increase the number of subbands.

Simulations and experimental measurements were used to establish the usefulness of the REC-FC technique in enhancing image contrast and reducing speckle noise for various targets with different contrasts and diameters. The results from simulations and experiments suggested that REC-FC was a useful tool to obtain substantial improvements in image contrast and to enhance the boundaries between the target and the background. CNR, $SSNR_B$, and $SSNR_T$ were increased in both simulations and experiments for all cases. Furthermore, in simulations and experiments, the overlap between the background and the target regions in the histograms of image intensity values was significantly reduced as the subbands decreased in width. lSNR increased in simulations

for all cases except the fourth-width case. However, lSNR from experiments suggested that pushing REC-FC to the third- and fourth-width cases may be unfavorable. In general, it was observed that REC-FC was always a step ahead of CP/CP-FC in terms of contrast improvement. This was due to the doubling of the axial resolution of the ultrasonic imaging system by using REC which allowed an increase in the number of subbands.

The REC-FC technique would require certain hardware infrastructure for an ultrasonic imaging system. The main component required would be an arbitrary waveform generator that can output the pre-enhanced chirp excitation signals. In addition, a digital signal processor is required in order to compress the received echoes. However, most ultrasonic imaging systems already contain digital signal processors, and versions capable of producing arbitrary waveforms on excitation are possible now. An additional experimental cost to using REC-FC in an ultrasonic imaging system is the requirement of acquiring the pulse-echo impulse response of the imaging system. Nonetheless, the approximate pulse-echo impulse response can be easily obtained by placing a known reflector at the focus of the source and exciting with a pulse.

3.2 Improving Quantitative Ultrasound using Coded Excitation Techniques

3.2.1 Introduction

In ultrasound a two-dimensional brightness image, known as a B-mode image, yields mostly qualitative information from a cross-section of the tissue being interrogated. These B-mode images are generated by digitally sampling radio-frequency signals backscattered from tissue which are then converted into a grayscale image by detecting the en-

velope. This process removes the frequency-dependent information contained in the backscattered radio frequency signal. However, additional quantitative information about the underlying tissue microstructure, structures that are smaller than the ultrasound wavelength, can be extracted from the frequency dependence of the backscattered radio frequency signals [63].

Quantitative ultrasound (QUS) imaging techniques based on ultrasonic backscatter have been used to characterize tissue and to successfully diagnose and monitor disease. Much of the theoretical foundation for tissue characterization using ultrasound spectral analysis was laid out by Lizzi et al. [63]. Applications where the frequency-dependent backscatter information was used to quantify tissues include ocular tumors [64–71], liver and kidney tissue characterization [71–75], prostate tumors [76, 77], breast tumors [78–84], and vascular abnormalities [85, 86]. These applications have established the potential importance of QUS in the ultrasonics community.

To model the scattering process for tissue characterization it is assumed that tissues conduct sound as an inhomogeneous fluid [87]. Furthermore, the model assumes scatterers of finite sizes that can be approximated by simple geometric shapes and therefore characterized by a size and concentration [82]. Moreover, the size and shape of the scatterers determine the magnitude at which a specific frequency of sound will be scattered [82]. Therefore, with QUS, the normalized backscattered power spectrum from a region of interest (ROI) can be parameterized and related to tissue microstructure [82]. For example, the effective scatterer diameter (ESD) and effective acoustic concentration of underlying scatterers can be estimated from the normalized backscattered power spectrum [82]. Parametric images can be constructed by associating the estimated scatterer properties with ROIs at different spatial locations. These ROIs correspond to pixels in the parametric image whose color or intensity corresponds to a particular parameter value. The size of the ROI corresponds to the spatial resolution of the parametric image and is dictated by the number of independent scan lines in the lateral extent and axially by the spatial distance delineated by a range gating function. By decreasing the sizes of the ROIs, the spatial resolution of the parametric image is improved. Unfortunately, a tradeoff exists between the accuracy and precision of the scatterer property estimates and the sizes of the ROIs [88]. Furthermore, one of the

most important factors reducing the effectiveness of QUS imaging techniques is the low contrast resolution between diseased tissues and normal tissues or between benign and malignant tumors. The contrast resolution of QUS images depends on the variance of QUS estimates. The variance of QUS estimates decreases with increasing bandwidth of the imaging system [82]. Therefore, an imaging system with larger bandwidth would yield lower variance in spectral estimates. A decrease in estimate variance will result in an increase of contrast resolution for QUS images.

The usefulness of parametric imaging for characterization and diagnosis of diseased tissue has improved due to the advancement of signal processing techniques that improve the accuracy of the estimates from backscatter. Recently, Kanzler and Oelze [89] improved QUS estimates of ESD in tissue-mimicking phantoms by using coded excitation and pulse compression. In that study, the increase in echo signal-to-noise ratio (eSNR) achieved through coded excitation resulted in increased depths (50%) at which accurate ESD estimates could be obtained versus conventional pulsing (CP) techniques. Kanzler and Oelze also observed that the coded excitation and pulse compression scheme had a minimal effect on the estimate variance because it reduced the estimate variance at a majority of depths by only a few percent.

The REC technique [18] was explored for improving both the bias and variance of QUS estimates, i.e., ESD estimates. The REC technique can increase the bandwidth of the ultrasonic imaging system by a factor of two without the presence of large sidelobes often observed with other coding and pulse compression techniques. In addition to the bandwidth enhancement, the REC technique has the typical coded excitation benefits, such as deeper penetration which is due to increases in the eSNR. Furthermore, a larger eSNR translates into a larger useable bandwidth of the imaging system. Usable bandwidth in this study of QUS imaging was defined as the segment of the backscattered power spectrum that is 6 dB above the noise floor. Chaturvedi and Insana [90] observed that the standard deviation in ESD estimates was inversely proportional to the bandwidth of the imaging system when using a spherical Gaussian model for scattering. Therefore, the goal of this study was to combine the REC technique with QUS, which will be described as REC-QUS, and evaluate the improvements in standard deviation of ESD estimates due to the enhanced bandwidth and gain in eSNR. Another goal was to

extend the tradeoff of estimate standard deviation and the spatial resolution of the parametric image (ROI size). Both a broadening of the bandwidth and gain in eSNR should yield improved QUS estimates, which in turn would improve the diagnostic capabilities of QUS imaging techniques for clinical applications.

3.2.2   Methods and procedures

QUS

The ESD can be estimated from the frequency dependence of the normalized backscattered power spectrum. To estimate the ESD from the normalized backscattered power spectrum, the following assumptions were made: multiple scattering was negligible, the scatterers were uniformly and randomly located spatially, and the distribution of scatterer sizes was small relative to the mean size. In soft tissues, the frequency dependence of the normalized backscattered power spectrum has been modeled by the acoustic intensity form factor, F, which is related to a 3D spatial autocorrelation function that describes the material properties of the scatterers [63,91]. For soft tissues, the theoretical power spectrum [91] is formulated by

$$P_{theor}(f) = B(L, q)C(a_{eff}, n_z)f^4 F(f, a_{eff}),\qquad(3.11)$$

where f is the frequency; B is a constant that depends on L, which is the axial length of the range gate, and on q, which is the ratio of the source radius to distance from the ROI; C is a constant depending on the average effective radius a_{eff} of the scatterers; and n_z is the effective acoustic concentration (product of the number density of scatterers times square of the relative impedance difference between the scatterers and surrounding tissues) [82].

The normalized power spectrum is calculated through [92]

$$P_{norm}(f) = \frac{A(f, L)}{N}\left(\frac{R}{2}\right)^2 \sum_{n=1}^{N} \frac{P_m(f)}{P_{ref}},\qquad(3.12)$$

where A is an attenuation compensation function, N is the number of gated scan lines in the ROI to be averaged, P_{ref} is a reference power spectrum, R is the reflectivity of

a planar surface used to obtain the reference power spectrum, and $P_m(f)$ is the power spectrum calculated from a range gated signal. The reference power spectrum, P_{ref}, was obtained by measuring the output of the transducer when a Plexiglas surface was positioned at the focus of the source [63].

QUS: Attenuation compensation

Frequency-dependent attenuation alters the shape of the power spectrum as attenuation increases with frequency. Hence, if the attenuation is not compensated for, the ESD will be overestimated. In simulations and experiments, a point compensation scheme was used. Point compensation [91] is described by

$$A_{pc}(f, x) = e^{4\alpha(f)R_1}, \tag{3.13}$$

where $\alpha(f)$ is the frequency-dependent attenuation and R_1 is the distance between the front-end of the object and the front-end of the the gated region.

QUS: Bandwidth

As previously stated, QUS techniques that make use of spectral information would be greatly improved by larger bandwidth imaging systems. Larger bandwidth leads to smaller variance in spectral estimates in QUS. Smaller variance in spectral estimates means that tissues will be more differentiable with QUS imaging techniques. The variance of ESD estimates when assuming a Gaussian form factor is inversely proportional to the bandwidth squared of the imaging system and is described by the following equation [82, 90]:

$$var\widehat{D} = \frac{2.09 \times 10^{-2}}{D^2} \left[\sum_{j=1}^{M} f_j^4 - M \cdot E\{f^2\}^2 \right]^{-1}, \tag{3.14}$$

where $\widehat{D}$ is the estimated ESD, D is the actual ESD in the ROI, f is frequency, f_j are frequency points in the analysis bandwidth that are uncorrelated, and M is the total number of data points used in the analysis bandwidth. Furthermore, (3.14) indicates that the variance in scatterer property estimates is inversely proportional to the ESD

squared. Note that although the expression in (3.14) is only true for monodisperse scattering ensembles, the bandwidth-variance relationship still holds for a distribution of scatterer sizes.

Computer simulations

Computer simulations were carried out in MATLAB (Mathworks, Natick, MA) to characterize the performance of the REC-QUS technique. The simulations used a received pulse-echo pressure field model [93] described as

$$g'[x, y, t] = h_1(t) * f(x, y) * h_{pe}(y, t), \qquad (3.15)$$

where x represents the axial spatial coordinate, y represents the lateral spatial coordinate, $f(x, y)$ is the scattering function, and $h_{pe}(y, t)$ is the modified pulse-echo spatial impulse response that takes into consideration the geometry of the transducer to the spatial extent of the scattered field (beam diffraction).

The pulse-echo impulse response, $h_1(nT, x)$, for CP was approximated by

$$h_1(t) = e^{-\frac{t^2 - \tau}{\sigma_t^2}} \cos(\omega t), \qquad (3.16)$$

where σ_t^2 is the second central moment of the Gaussian pulse which dictates the bandwidth of the pulse. A shift, τ, was added to $h_1(t)$ to make the pulse causal. The generated pulse-echo impulse response was located at the focus of a 10 MHz single-element transducer (f/4) with a -6 dB fractional bandwidth of 80%.

For REC, the impulse response function, $h_2(t)$, was constructed to have a -6 dB fractional bandwidth of 150% by gating a sinusoid of four cycles with a Hanning window

$$w(n) = \begin{cases} 0.5(1 - \cos(\frac{2\pi n}{L_H - 1})), & 0 \leq n \leq L_H - 1 \\ 0, & \text{otherwise,} \end{cases} \qquad (3.17)$$

where n is an integer and L_H is the number of samples in the window. A Hanning window of length $L_H = 24$ was used.

The spatial response for a circular focused piston source was simulated as a circular

Gaussian beam which is defined as

$$h_{pe}(y,t) = \delta(t - \frac{2R_d}{c})e^{\frac{-y^2}{\sigma_y^2}} , \tag{3.18}$$

where R_d is the distance from the source to target in space, c is the speed of sound of the medium which was set to 1540 m/s, and σ_y is the -6 dB lateral beamwidth which is equal to 0.62 mm.

Three different phantom types, S1, S2, and S3 were simulated. Ten simulations were performed for the first two types of phantoms, S1 and S2, while one simulation of the third type, S3, was performed. Descriptions of the first two simulated phantoms are shown in Table 3.13. Descriptions of the third phantom are shown in Table 3.14. Phantoms S1, S2, and S3 contained an average of 15 point scatterers per resolution cell volume. These scatterers had an f^4 dependence on the backscattered power spectrum. However, to model soft tissue scattering and to obtain ESD estimates, the simulated phantoms were modified by the spherical Gaussian form factor [91]. The spherical Gaussian form factor was used to model soft tissue scattering which is described by

$$F_{Gauss}(f) = e^{-12.159f^2 a_{eff}^2}. \tag{3.19}$$

The spherical Gaussian form factor has been used by various researchers to model the scattering of soft tissues [66, 82, 91, 94–96]. In addition, the backscattered data was reduced by the frequency-dependent attenuation corresponding to the distance of the scatterer from the source. The attenuation was set to 0.5 dB MHz^{-1} cm^{-1}. Phantom S1 was used to evaluate the effects that REC had on the spatial resolution of QUS images due to the increase in bandwidth. Phantom S2 consisted of the same parameters of phantom S1 except that it contained a cylindrical lesion of 6 mm radius that was centered in a background region. Phantom S2 was used to evaluate the effects of REC on the contrast resolution of QUS images due to the improvements in standard deviation of ESD estimates. Phantom S3 consisted of the same parameters of phantom S2 except that it contained three cylindrical lesions of 6 mm radius. Phantom S3 was used to evaluate the contrast resolution achievable from lesions with different scatterer diameters that were imaged with the same source. Phantoms S1, S2, and S3 were placed

40 mm from the simulated source which had a focal depth of 50 mm.

The backscatter coefficient estimates [92] were obtained by

$$\sigma_b(f) = \frac{3.87(R_0 + R_1)^2}{A_o L} P_{norm}(f), \qquad (3.20)$$

where A_o is the surface area of the transducer, R_0 is the on-axis distance between the transducer and the front-end of the object being imaged, and R_1 is the distance between the front-end of the object and the front-end of the the gated region. From the frequency dependence of the backscatter coefficient the parametric images of ESD can be obtained.

The received simulated radio frequency backscatter data were sampled at a rate of 100 MHz and the transducer was translated laterally in increments of 0.31 mm (50% beam overlap). For phantom S2 and S3, the sizes of ROIs were selected based on recommendations from previous analysis of ROI versus estimate bias and variance [88]. Axially, individual scan lines were gated with a rectangular window of a length corresponding to 5.5 CP axial pulse lengths. Laterally, a distance of five lateral beamwidths was used, corresponding to 10 scan lines because data were acquired with a 50% beamwidth overlap between scan lines. Therefore, each ROI was a rectangle 1.52 mm x 4.15 mm. However, ROIs were overlapped both laterally and axially by 66%; therefore, the effective ROI size after averaging was 0.50 mm x 1.38 mm. For phantom S1, the size of the ROI was varied in the axial extent as the goal of this study was to evaluate the estimate bias and standard deviation as a function of gate length.

Estimates of ESD were obtained by approximating the measured power spectrum by a best-fit line technique [82]. Specifically, estimates were obtained by comparing the logarithm of the measured backscattered power spectrum (3.12) with the logarithm of the theoretical power spectrum (3.11) through the equation,

$$10 \log_{10} P_{norm}(f) - 10 \log_{10} f^4 \approx m(a_{eff})f^2 + b(n_z, a_{eff}, L, q). \qquad (3.21)$$

Equation (3.21) describes a straight line, $y = mx + b$ where $x = f^2$, m is the slope and is a function of a_{eff}, and b is the intercept and is a function of a_{eff}, n_z, q, and L. Finally, estimates were obtained by using least-squares analysis to find the best-fit line to the

measured and processed data from (3.21) using an analysis bandwidth corresponding to the -6 dB bandwidth of the simulated source.

Experimental Setup

Scatterer property estimates from experiments were obtained to validate the improvements afforded by the REC-QUS technique in an experimental setting. A single-element weakly-focused (f/4) transducer with a center frequency of 10 MHz was used to image phantoms by translating the transducer laterally across the phantom. The transducer had a -6 dB pulse-echo bandwidth of 80% along with a -6 dB pulse-echo beamwidth of 0.67 mm. These parameters were estimated using the wire technique [97] for transducer characterization. Using REC the -6 dB pulse-echo bandwidth was enhanced to 155%. There were two different experimental setups utilized; one for CP and another one for REC experiments. These setups would contain different noise levels due to the use of different excitation systems. Therefore, to avoid errors in the comparisons, the noise levels were normalized so that they contained the same eSNR before compression. Normalization of eSNR was accomplished by adding zero-mean white Gaussian noise to the CP radio frequency echo waveforms because REC had the lower eSNR before compression. The two experimental setups are described by Fig. 3.24.

1. Conventional pulsing experimental setup: The transducer was excited by a pulser-receiver (Panametrics 5900, Waltham, MA) which was connected to a Ritec diplexer (Warwick, RI). The echo waveform was received by a different pulser-receiver (Panametrics 5800, Waltham, MA) which then was displayed on an oscilloscope (Lecroy 9354 TM, Chester Ridge, NY) for visual verification. The echo signal was recorded at a rate of 100 MHz by a 12-bit A/D (Strategic Test Digitizing Board UF3025, Cambridge, MA) for further processing by a PC. A diagram of the experimental setup for CP is shown in Fig. 3.24.

2. REC experimental setup: The pre-enhanced chirp was generated in MATLAB and downloaded to an arbitrary waveform generator (Tabor Electronics W1281A, Tel Hanan, Israel). The excitation signal was amplified by a radio frequency power amplifier (ENI 2100L, Rochester, NY). The amplified signal (50 dB) was

67

connected to the transducer through a diplexer (Ritec RDX-6, Warwick, RI). The echo signal was received by a pulser-receiver (Panametrics 5800, Waltham, MA), which was displayed on an oscilloscope (Lecroy 9354 TM, Chester Ridge, NY) for visual verification. The echo signal was recorded at a rate of 100 MHz by a 12-bit A/D (Strategic Test Digitizing Board UF3025, Cambridge, MA) for further processing by a PC. A diagram of the experimental setup for REC is shown in Fig. 3.24.

Measurements from four physical phantoms were obtained to evaluate the performance of REC-QUS versus conventional QUS methods. Descriptions of the four physical phantoms used in the experiments are shown in Table 3.15 and Table 3.16. The phantoms were cylindrical samples bounded within an acrylic housing that contained a 25 μm Saran Wrap plastic film (Dow Chemical, Midland, MI) [98] on the parallel flat surfaces. The Saran Wrap layer served as a window for transmission of the ultrasound waves between water and the tissue-mimicking phantom. Therefore, to obtain correct estimates of phantom parameters the frequency-dependent transmission coefficients of the Saran Wrap layers need to be compensated. The transmission coefficient for a single layer of Saran Wrap is given by [98]

$$T(k) = \frac{2Z_f}{(Z_i + Z_f)\cos(k_{saran}l) + j(Z_{saran} + \frac{Z_i Z_f}{Z_{saran}})\sin(k_{saran}l)}, \qquad (3.22)$$

where Z_i is the acoustic impedance of the incident material ($Z_i = 1.49$ MRayls), Z_f is the acoustic impedance of the final material ($Z_f = 1.49$ MRayls), and Z_{saran} is the acoustic impedance of the Saran Wrap layer of length l. k_{saran} is the wave number in the layer and is described by

$$k_{saran} = \frac{2\pi f}{c_{saran}} - j\alpha(f), \qquad (3.23)$$

where c_{saran} is the speed of sound and α the frequency-dependent attenuation coefficient of the Saran Wrap layer. More information about phantoms A and B can be found in [98]; likewise, more information about phantoms C and D can be found in [99].

The received radio frequency backscatter data were sampled at a rate of 100 MHz and the transducer was translated laterally in increments of 0.33 mm (50% beam overlap).

The sizes of ROIs were again selected from recommendations of appropriate ROI size versus estimate bias and variance [88]. Axially, individual scan lines were gated with a rectangular window of a length that would correspond to 15 CP axial pulse lengths. Laterally, five lateral beamwidths were used, which corresponds to 10 scan lines because data were acquired with a 50% beamwidth overlap between scan lines. Therefore, each ROI was a rectangle 3.3 mm x 3 mm. However, ROIs were overlapped both laterally and axially by 66%; therefore, the effective ROI size after averaging was 1.1 mm x 1 mm.

Estimates of ESD were obtained by minimizing the average squared deviation (MASD) as a function of ESD,

$$\widehat{D} = \min_{ASD}(E\{(X(f, ESD) - E\{X(f, ESD)\})^2\}), \tag{3.24}$$

where $X(f, ESD)$ is $10\log_{10}(\sigma_b/\sigma_0)$. σ_0 is the theoretical backscatter coefficient obtained from Faran's theory [100, 101] and σ_b is the backscatter coefficient from the phantom. σ_b was estimated by using a broadband substitution method for weakly focused transducers [92]. Estimates of the backscatter coefficient were obtained using Eq. (3.20). The mean of $X(f, ASD)$ was subtracted from $X(f, ASD)$ because the ESD estimate depends only on the frequency dependence of the backscatter coefficient and not the magnitude.

During experiments, large echoes from the front surface of the phantoms were clipped because the A/D card had a voltage limitation of ± 0.5 V. This was an engineering tradeoff because gain was applied so that the backscatter behind the front surface fully spanned the dynamic range of the A/D card. However, a consequence of clipping AM and FM modulated signals is that after compression large sidelobes are introduced. As a result, the portion of the signal that was being clipped was replaced with zero-mean white Gaussian noise that contained the same variance introduced by the system [89].

In measurements, the phantoms were placed in a tank of 20 °C degassed water such that the fronts of the phantoms were perpendicular to the beam axis of the transducer as shown in Fig. 3.25. Measurements of backscatter for all phantoms were obtained for three distances of R_1: 10 mm, 15 mm, and 20 mm. Each distance represents a shift in the placement of the focus within the phantom. R_0 was decreased by the same amount R_1 was increased in order to maintain the sum of R_0 and R_1 constant. QUS parametric

images for experimental measurements were generated by compounding the estimates for all three distances listed above. Reference pulses were obtained by reflecting an incident pulse off a Plexiglas surface for both CP and REC. Because estimates require a normalization with a reference spectrum that is located at the center of the gate, reference pulses were obtained in increments of 500 μm that spanned the entire depth-of-focus.

Quality metrics

To assess the REC-QUS technique, numerical simulations were implemented, and experimental measurements were acquired. The simulations and experiments used REC to increase the -6 dB bandwidth of the imaging system for QUS analysis and results were compared to CP methods. Therefore, to evaluate the performance of the REC-QUS technique against CP the following quality metrics were used:

1. Standard deviation: Estimate standard deviation quantifies the estimation precision and is arguably the most important metric of QUS imaging. The main limitation of QUS imaging techniques when differentiating and characterizing tissues is the overlapping of estimate values due to the size of estimate standard deviation. By reducing estimate standard deviation, QUS imaging techniques will be more sensitive to tissue differences and improve diagnostic capability.

2. Bias: Estimate bias is the deviation of the simulated or measured QUS parameter from a reference scatterer diameter. The accuracy of the underlying structure was quantified by the bias of the scatterer property estimates. However, when evaluating the experiments with physical phantoms, estimate mean was used over estimate bias because the phantoms contained scatterers with varying diameters. In these cases, the out of range, i.e., the percentage of size estimates that were not bounded between the maximum and minimum scatterer diameter, were tallied to obtain a measure of correctness of estimation (estimates that do not deviate from the range).

3. Contrast-to-noise ratio (CNR): CNR is a quantitative measure that was used to assess image quality and describe the ability to perceive a lesion from the

background region or lesion-free region. CNR [34] is defined as

$$CNR = \left| \frac{\mu_B - \mu_L}{\sqrt{\sigma_B^2 + \sigma_L^2}} \right| \tag{3.25}$$

where μ_B and μ_L are the mean brightness of the background and the target lesion and σ_B^2 and σ_L^2 are the variance of the background and target, respectively. To avoid possible errors in the calculations due to attenuation, the evaluated ROIs in the background and the target lesion were of the same size and located at the same depth. CNR is a unitless quantity.

4. Histogram overlap: Histogram overlap is the percentage of pixels in the background and target lesion histograms that share the same pixel intensity. Histograms were made for same-sized regions for the target lesion and the background adjacent to the target. Like CNR, the histogram overlap is a measure of the detectability of the lesion from the background. Note that the number of points in the histograms varied based on the sizes of the ROIs.

3.2.3   Results

Simulations

The results form simulations of phantom S1 consisted of estimates obtained with varying sizes of the axial gate. The axial gate lengths evaluated for CP and REC were dictated by the pulse length at -15 dB. One CP pulse length corresponded to 0.277 mm while for REC one pulse length corresponded to 0.169 mm. The bias and standard deviation of ESD estimates for phantom S1 are shown in Fig. 3.26.

Simulations of phantom S2 consisted of obtaining ESD estimates for the target lesion and the background region. The purpose of this simulation was to evaluate the quality of REC-QUS parametric images when two simulated tissues have a small difference in ESD values. Changes in standard deviation of ESD estimates were obtained by varying the size of the axial gate with the simulations of phantom S2. For this study, the image quality metrics were the CNR and the histogram overlap, which were generated by assessing the lesion and background regions of the QUS parametric images. For a gate

length corresponding to the 15 REC pulse lengths (2.54 mm), the CNR was 1.28 ± 0.52 for CP and 2.47 ± 0.42 for REC. Comparisons of CNR as a function of CP pulse lengths for phantom S2 are shown in Fig. 3.27.

Histogram analysis further highlighted the improvements obtained by using REC-QUS over conventional QUS. CNR allowed quantification of the improvement in contrast while histogram overlap was used to evaluate the overlap in intensity between QUS pixels in the lesion and background regions. In addition, histogram overlap allowed quantification of the optimal gate length when examining the tradeoff between axial resolution and contrast resolution. Note that analysis of the overlap regions did not contain ROIs that were near the perimeter of the lesion. Histogram overlap as a function of pulse length for phantom S2 is shown in Fig. 3.27.

Conventional B-mode images for phantom S2 are shown in Fig. 3.28. The CNR values for the B-mode images of CP and REC shown in Fig. 3.28 were both 0.14. The parametric images for the QUS estimates of ESD for the following axial gate lengths: 0.61 CP pulse lengths (1 REC pulse length), 3.05 CP pulse lengths (5 REC pulse lengths), 6.10 CP pulse lengths (10 REC pulse lengths), and 9.15 CP pulse lengths (15 REC pulse lengths), are shown in Figs. 3.29. Histograms corresponding to these are shown in Figs. 3.30. Bias, standard deviation, histogram overlap and CNR for the parametric images shown in Figs. 3.29 and the values versus CP pulse length are listed in Table 3.17-3.18.

Simulations of phantom S3 consisted of obtaining ESD estimates for the target lesions and the background region. The purpose of this simulation was to evaluate the quality of REC-QUS parametric images when using one source for imaging simulated tissues with different ESDs (30, 60 and 90 μm) with respect to a background medium (50 μm). For this study, the image quality metric utilized was CNR. CNR values were generated by assessing the lesion and background regions of the QUS parametric images. Conventional B-mode images for phantom S3 are shown in Fig. 3.31. The parametric images for the QUS estimates of ESD are shown in Fig. 3.32. CNR results for the axial length [88] of 15 REC pulse lengths (2.54 mm) along with the standard deviation of the ESD estimates are shown in Table 3.19.

Experiments

B-mode images for CP and REC along with a parametric image overlay for all phantoms are shown in Fig. 3.33. Furthermore, the ESD and standard deviation of ESD estimates as a function of depth for all phantoms are shown in Fig. 3.34. The results for out of range and standard deviation of ESD estimates for all depths combined are shown in Table 3.20.

The ESD results in Fig. 3.34 demonstrate that REC-QUS obtained improved estimates when compared to conventional QUS methods using CP. Moreover, the standard deviation of ESD estimates in Fig. 3.34 corroborate that improvements in standard deviation were obtained by increasing the useable bandwidth through REC. Furthermore, by using REC over CP a decrease in the standard deviation of ESD estimates of 34%, 75%, and 71% were obtained for phantoms A, C, and D, respectively.

3.2.4   Discussion and conclusions

Simulations

For phantom S1, the bias results in Fig. 3.26a demonstrated that REC-QUS obtained improved estimates when compared to conventional QUS methods using CP. Additionally, the standard deviation results in Fig. 3.26b provided evidence that the bandwidth enhancement generated by using REC resulted in significant improvements in estimation error. For ROIs of CP axial pulse lengths of one through four, a mean decrease of 52% in standard deviation was obtained by using REC. Furthermore, by using REC over CP an approximate 43% decrease in the standard deviation of ESD estimates was obtained for ROIs with axial pulse lengths greater than four. More importantly, standard deviation when obtaining estimates with an axial length of 15 CP pulse lengths was 7.09 for CP. For REC the same standard deviation was achieved with an axial length of 1.33 CP pulse lengths. These results suggest that the same standard deviation obtained with conventional QUS can be achieved by using REC-QUS but with a smaller axial pixel size for the parametric image. In fact, the axial pixel in the parametric image would be approximately less than twice the size of the axial pixel length in a conventional B-mode image.

For phantom S2, fitting the CNR data of Fig. 3.27 with a line in the least-squares sense provided a slope of 0.09 and an intercept of 0.41 for CP, while a slope of 0.20 and an intercept of 0.64 was obtained for REC. These results suggested that a greater increase in contrast occurred using REC, in addition to an improvement in axial resolution. In fact, REC-QUS parametric images achieved an average of 38% increase in contrast when compared to the conventional QUS parametric images generated using CP. Furthermore, observation from Fig. 3.27 indicates that for REC-QUS, histogram overlap reached approximately 0% for a gate length of 9.5 CP pulse lengths, while for conventional QUS 0% was achieved at 17.3 CP pulse lengths. These results indicate that the optimal axial gate length, where the parametric image using REC yielded optimal contrast, was around 10 CP pulse lengths. By using REC-QUS with a gate length of 10 CP pulse lengths as opposed to conventional QUS with a gate length of 17 CP pulse lengths, a gain of 70% in axial resolution in the parametric image was achieved.

Examination of the REC parametric images in Figs. 3.29 reveals that by using REC-QUS the lesion was more clearly observed in all cases when compared to conventional QUS methods for the same gate length. The contrast increased as the gate length increased. Furthermore, histogram analysis extended the notion of improved contrast and target detectability by illustrating the increased separation between the target and background as the gate length increased. These observations were supported by the improvements in contrast and reduction of histogram overlap as shown in Fig. 3.27. CNR results indicated that with both REC-QUS and conventional QUS an improvement in contrast can be achieved when compared to the conventional B-mode images shown in Fig. 3.28. Moreover, the decrease in histogram overlap using REC-QUS led to improved detection and differentiation of the lesion from the background when compared to CP.

A further benefit of REC-QUS is observed by comparison of the bias and standard deviation for the background regions in REC and CP as shown in Table 3.17 and Table 3.18. For example, for ROIs of 15 REC pulse lengths (9.15 CP pulse lengths) [88], the bias for CP was -3.76 μm for the background and -2.01 μm for the lesion while the bias for REC was 2.71 μm for the background and -7.28 μm for the lesion. Similarly, the standard deviation for ROIs of 15 REC pulse lengths (9.15 CP pulse lengths) for CP was 6.89 μm for the background and 5.41 μm for the lesion while for REC the standard

deviation was 2.66 μm for the background and 2.08 μm for the lesion. These results suggest that for conventional QUS the standard deviation of ESD deteriorated as the diameter of the scatterer decreased. Conversely, using REC the performance of QUS was increased because it resulted in accurate estimates for a smaller scatterer diameter due to the large ka range obtained by increasing the useable bandwidth. This larger ka range suggests that by using REC-QUS, scatterers with different diameters could be quantified by using the same transducer as opposed to conventional QUS where multiple source may be needed.

Recall that the difference in scatterer diameter between the lesion and the background was 10 μm for phantom S2. The small difference in scatterer diameter was evaluated to establish the tradeoff between axial length and standard deviation. Figure 3.29(a) has poor contrast when compared to Fig. 3.29(d); however, the axial pixel length was the same as the B-mode image in Fig. 3.28, which would allow smaller targets to be detected. Conversely, Fig. 3.29(d) has good contrast when compared to Fig. 3.29(a). However, the axial pixel length was 15 times the axial pixel length of the B-mode image in Fig. 3.28. As a result, this axial pixel length provided a smooth high contrast image but at the expense of potentially not detecting smaller targets. Naturally, targets could be easily detected if the difference in scatterer diameter were larger. In summary, the studies with phantom S2 suggested that REC-QUS could be used to extend the tradeoff between axial length and contrast to improve target detectability.

For phantom S3, the results in Table 3.19 indicate that REC-QUS obtained improved results over CP in terms of CNR. Specifically, for the 30 μm scatterer diameter lesion, the CNR improved by 45%. For the 60 μm and the 90 μm scatterer diamter lesions, the improvements increased to 152%. In terms of estimate standard deviation, REC obtianed improved results over conventional QUS by 77%, 90%, and 62% for the 30, 60, and 90 μm scatterer diameter lesions, respectively. A lateral profile of the parametric image in Fig. 3.32 is shown in Fig. 3.35. This profile illustrates how closely REC-QUS tracks the actual scatterer diameter and how CP failed to obtain accurate estimates as the scatterer diameter became smaller. The significance of these results lies in the fact that contrast improvements and reduction of estimated standard deviation were achieved by using one source instead of multiple sources. Multiple sources with different

center frequencies could be used to obtain ka ranges that might be optimal to the ESD estimates in phantoms. However, by using REC the ka range increased significantly to the point that targets with various scatterer diameters could still be evaluated with minimum estimation error.

Experiments

The ESD results in Figs. 3.34 demonstrated that REC-QUS had a better ability to obtain improved estimates when compared to conventional QUS methods using CP. Moreover, the standard deviation of ESD estimates in Figs. 3.34 corroborates that improvements in standard deviation were obtained by increasing the useable bandwidth through REC. Furthermore, by using REC decreases in the standard deviation of ESD estimates of 34%, 75%, and 71% were obtained for phantoms A, C, and D, respectively, compared to CP.

The standard deviations from combining all QUS ESD estimates for phantom B (Table 3.20) were 9.6 for CP and 10.9 for REC. At first glance, for this particular phantom these results suggest that conventional QUS was preferable over REC-QUS. Evaluating the results in Fig. 3.34(b), the standard deviation of REC-QUS was always lower than conventional QUS by using CP at any particular depth. However, analysis using Fig. 3.33(b) along with Fig. 3.34(b) helps explain why the standard deviation of QUS ESD estimates using all depths combined was larger for REC than for CP. In REC-QUS the ESD decreased as the depth increased, causing a large standard deviation when calculating the standard deviation from all depths combined. As a consequence, conventional QUS had a better overall standard deviation but a poor predictive ability because the majority of estimated values were out of the range of scatterers in the phantom.

Overall, as the penetration depth increased, the improvements in the standard deviation of ESD estimates using REC increased. This improvement was due to the increase in eSNR by using coded excitation and the increase in the bandwidth. REC-QUS resulted in more accurate ESD estimates because REC-QUS obtained a larger percentage of estimates that were within the true range of scatterer diameters.

REC-QUS extended the results by Kanzler and Oelze [89]. In [89], improved es-

timation bias versus penetration depth was obtained because of the increase in eSNR by using coded excitation. REC can achieve similar results as it produces an increase in eSNR by exciting the source with a pre-enhanced chirp. Moreover, the extension to their work comes from using the pre-enhanced chirp, which also increased the useable bandwidth by a factor of two. Therefore, the results were extended by combining REC with QUS techniques as the larger useable bandwidth resulted in a reduction in the standard deviation of ESD estimates. Smaller standard deviations aid in the classification of tumors and tissue typing.

Previous studies have indicated that simple QUS techniques can differentiate between different kinds of tumors in animal models of cancer [83,84]. Specifically, a study by Oelze and Zachary [83, 84] evaluated conventional QUS techniques *in vivo* on mice with transplanted 4T1 mammary carcinomas and EHS sarcomas. The objective of the study was to classify the two types of tumors. However, estimates of ESD and effective acoustic concentration contained a significant amount of overlap. Furthermore, in that study statistical differences were only observed when the bandwidth was limited to certain regions of the power spectra. By having more available bandwidth for estimates, it is more likely that with REC-QUS regions of bandwidth could be chosen that would yield estimates that produce statistically significant differences. Therefore, in pre-clinical and clinical settings, REC-QUS has a greater potential to markedly improve the differentiation between these different types of tumors because of the reduced estimate variance, lesion-to-background contrast, larger ka range, and smaller axial pixel length. A significant advantage that REC-QUS has over conventional techniques is that because of the increased available bandwidth, different scales of structure may be observed because of different scales of structure dominate the scattering at different frequencies. In other words, REC-QUS has the potential to assess tissues using multiple scales with one source as opposed to conventional QUS techniques where multiple sources with different center frequencies may be needed.

A potential limitation of REC-QUS is the fact that sources with larger bandwidth tend to have a large center frequency shift due to the frequency-dependent attenuation. Besides the center frequency shift, a decrease in the -6 dB bandwidth is encountered which would effectively reduce the variance improvements obtained with REC-QUS.

However, if bandwidth is defined as the 6 dB level above the noise, REC-QUS will still provide a larger bandwidth for analysis. Furthermore, it should be noted that Phantom C and Phantom D contained scatterers in the range of 45 to 53 μm diameter but with different attenuation coefficients 0.5 and 0.8 dB MHz^{-1}cm^{-1}, respectively. Therefore, because of the higher attenuation coefficient in Phantom D, the standard deviation of the ESD estimates increased by 18% when using REC-QUS. As a comparison, with conventional QUS a 1% increase in the standard deviation of the ESD was observed. Nonetheless, a 70% decrease in the standard deviation of ESD was obtained when using REC-QUS over conventional QUS.

3.3 Figures and Tables
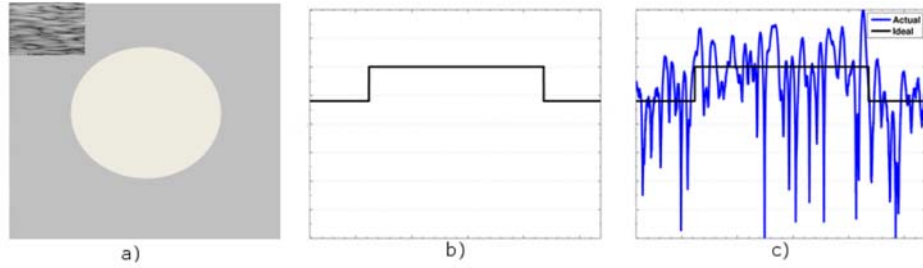
Figure 3.1: Example showing what speckle does to an ultrasound image. (a) An ideal image of a lesion (except the upper left corner which shows a region full of speckle), (b) the axial profile of the ideal lesion (the ideal scan line), (c) the resulting scan line after the lesion is scanned with ultrasound.
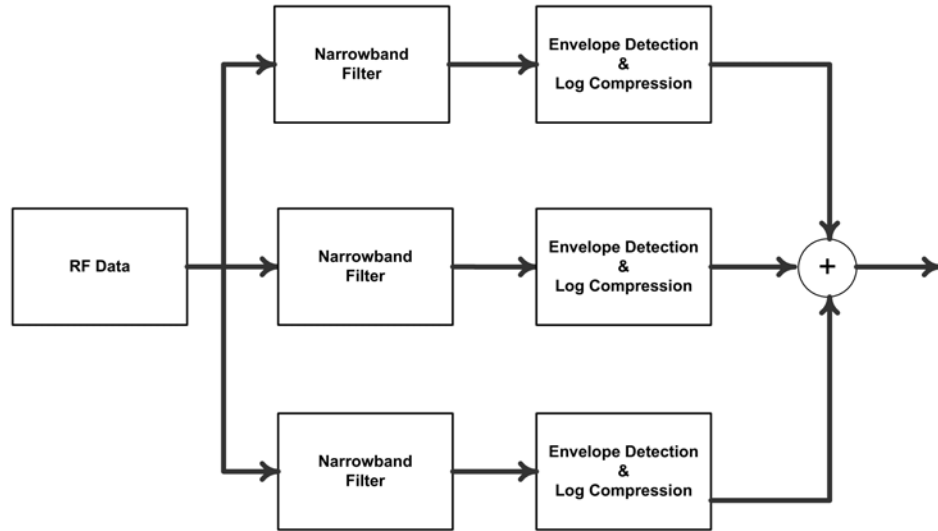
Figure 3.2: Block diagram of an FC scenario with three subbands. Each subband consists of a narrowband filter that contains a different center frequency when compared to other subbands.

Reference B-mode

Subband filters
with RF-data

B-modes generated
from each subband

Compounded B-mode

B-MODE
IMAGE

Axial Distance [mm]

Lateral Distance [mm]

Normalized Amplitude

AMPLITUDE/
FREQUENCY
PLOT

Frequency [MHz]
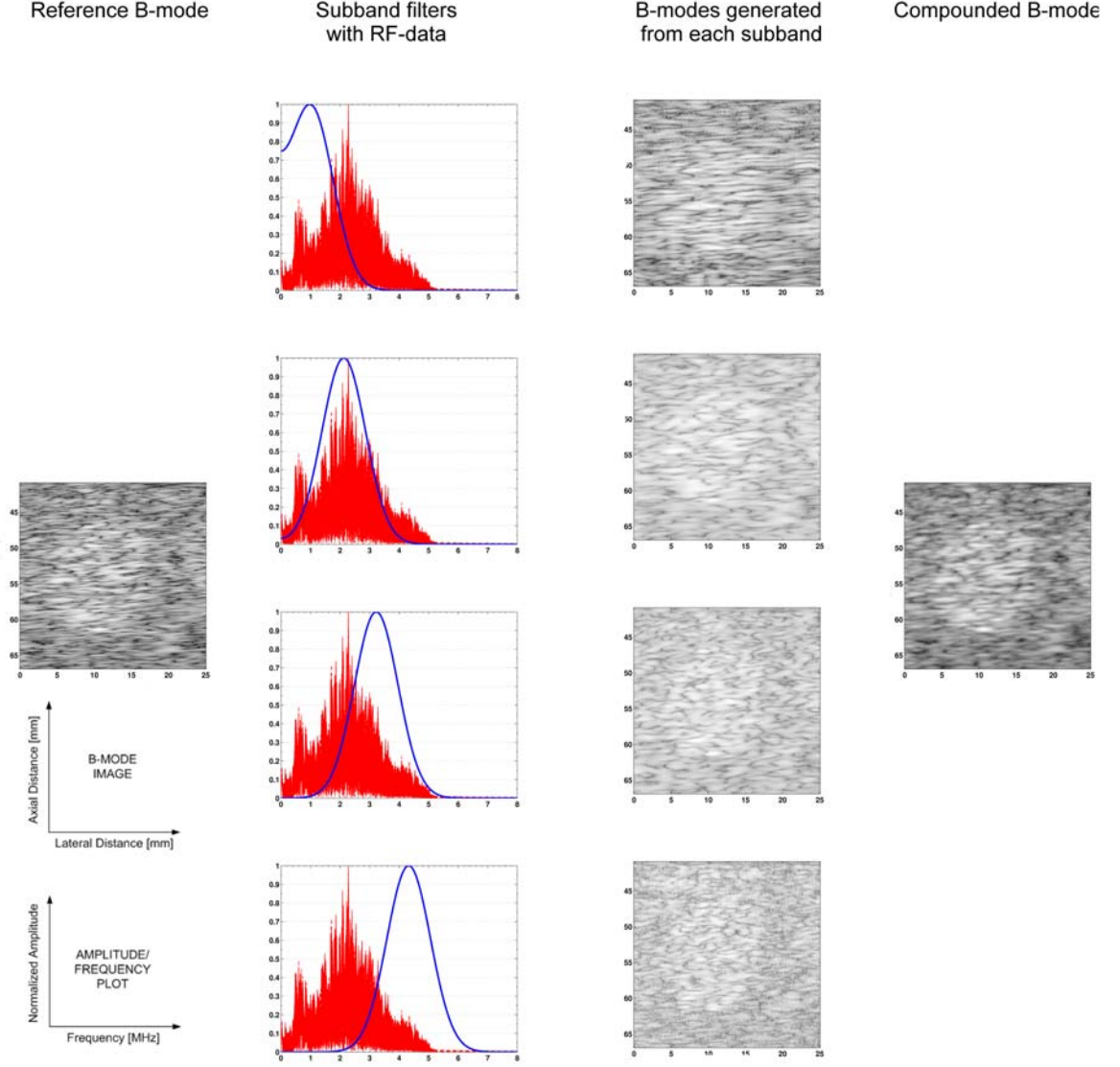
Figure 3.3: The first column shows the B-mode image from the REC reference. The second column shows the partitioning of RF-data with Gaussian subbands. The third column shows the B-mode images with partially uncorrelated speckle patterns. These B-mode images were generated by taking the envelope and log-compressing the RF output from each subband. The final column shows the compounded B-mode image with improved contrast.

80
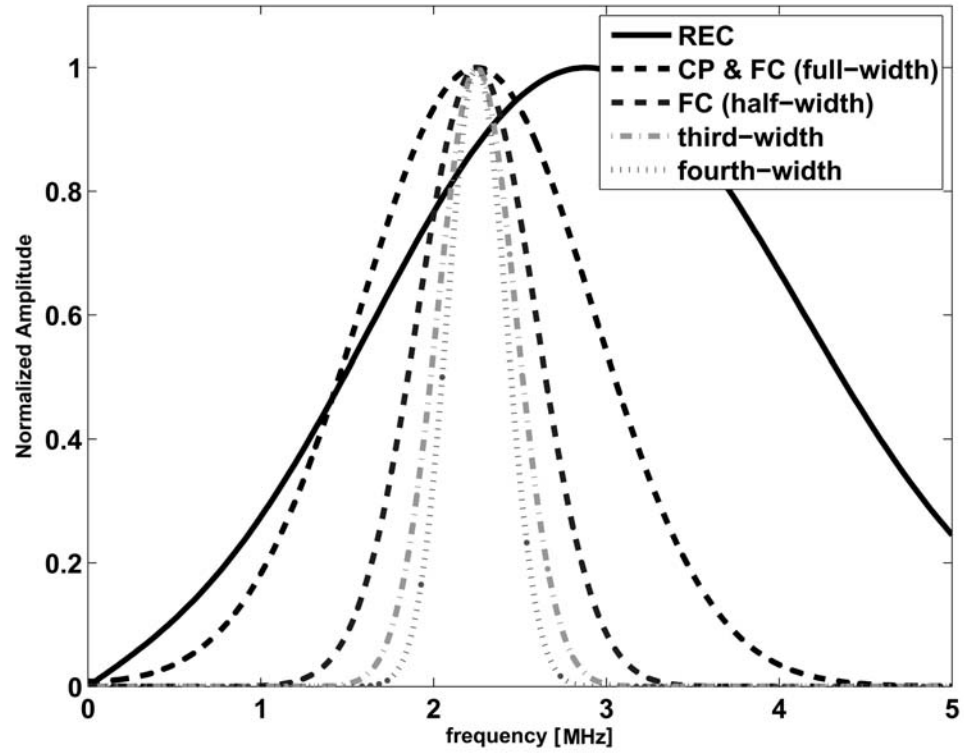
Figure 3.4: Illustration of the bandwidth for all four FC cases applied in conjunction with the bandwidth of the reference signals for CP and REC. Note: REC center frequency was shifted to eliminate any dc-component in the spectrum.
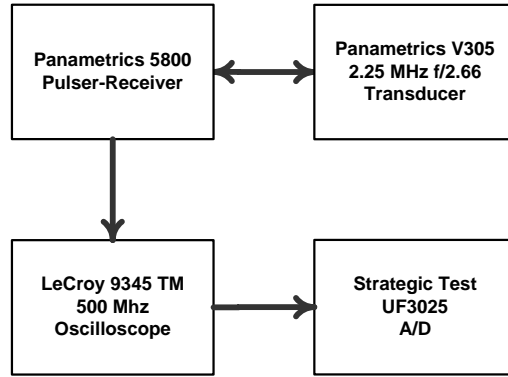
(a)
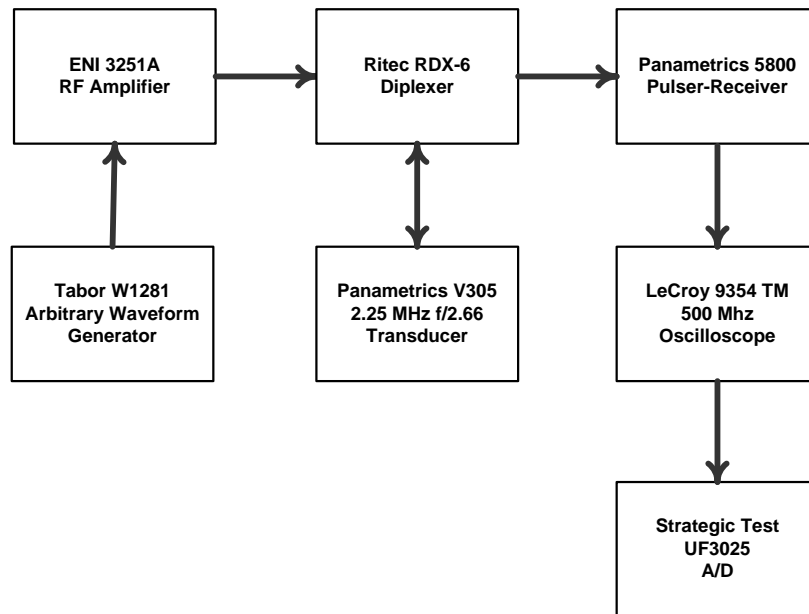
(b)

Figure 3.5: (a) Block diagram of experimental setup for CP, and (b) block diagram of experimental setup for REC.
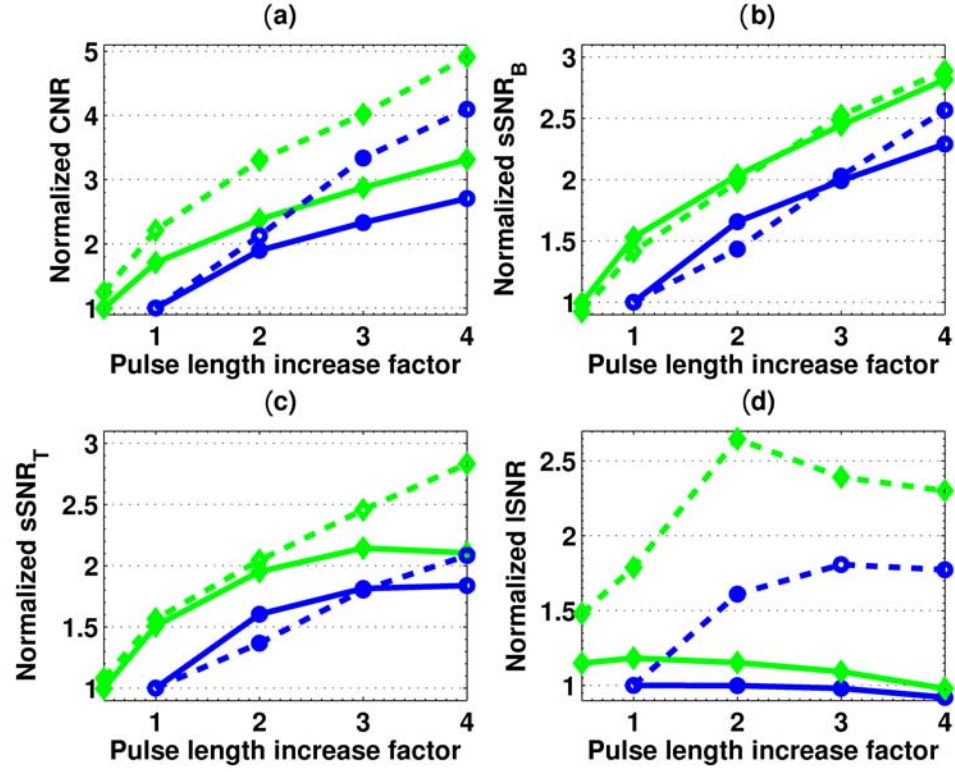
Figure 3.6: (a) Normalized CNR vs. pulse length increase factor, (b) normalized $sSNR_B$ vs. pulse length increase factor, (c) normalized $sSNR_T$ vs. pulse length increase factor, (d) normalized lSNR vs. pulse length increase factor. For simulations and experiments, the quality metric values were normalized to the data corresponding to conventional pulsing with a pulse length increase factor of one. (Simulated results are depicted by a solid line, experimental measurements are shown in a dashed line, REC results are marked by diamonds, and CP results are marked by circles.)
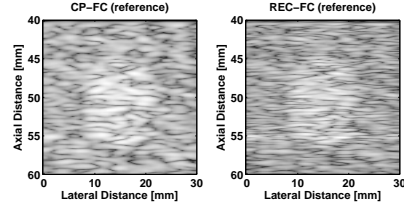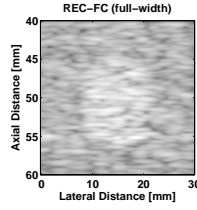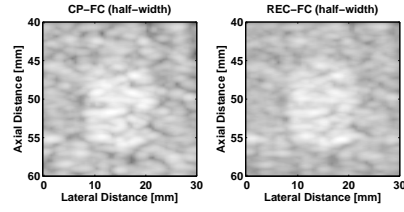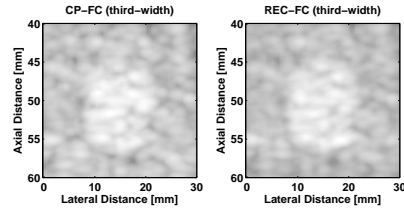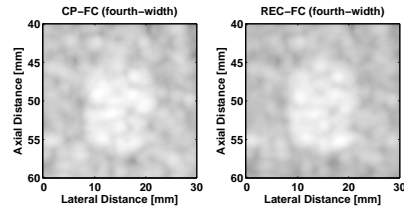
Figure 3.7: B-mode images of simulated results for: (a) CP and REC reference scans, (b) REC-FC full width case, (c) CP-FC and REC-FC half-width cases, (d) CP-FC and REC-FC third-width cases, and (e) CP-FC and REC-FC fourth-width cases. Image dynamic range = -50 dB.
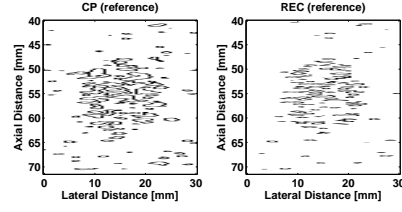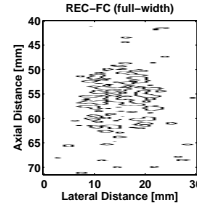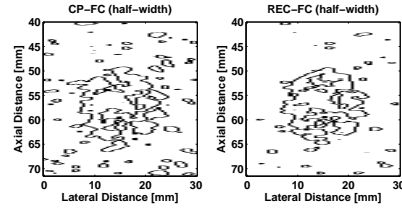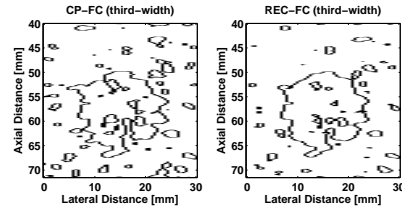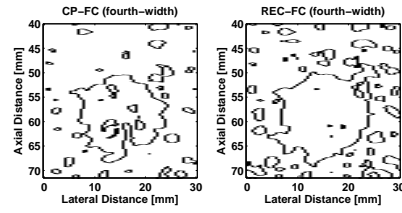
Figure 3.8: Edge detection images of simulated results using thresholding and margin strength for: (a) CP and REC reference scans, (b) REC-FC full width case, (c) CP-FC and REC-FC half-width cases, (d) CP-FC and REC-FC third-width cases, and (e) CP-FC and REC-FC fourth-width cases.
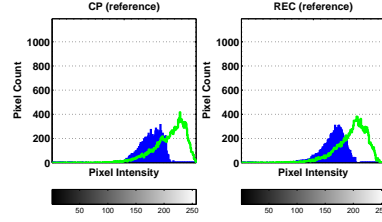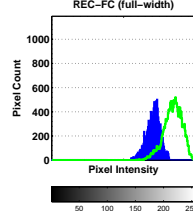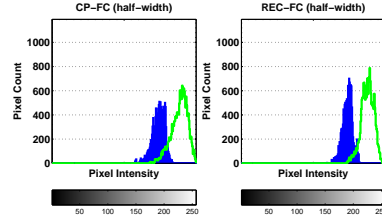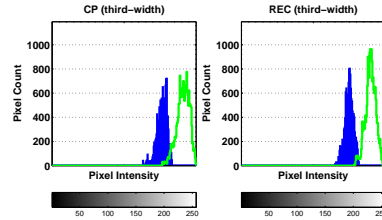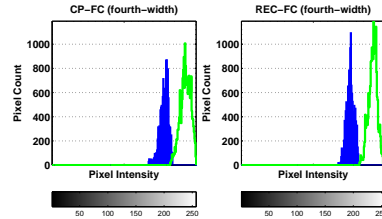
Figure 3.9: Histograms of simulated results for: (a) CP and REC reference scans, (b) REC-FC full width case, (c) CP-FC and REC-FC half-width cases, (d) CP-FC and REC-FC third-width cases, and (e) CP-FC and REC-FC fourth-width cases. The pixel intensity is represented by the grayscale bar shown underneath the plot. (Color: background region is blue, and target region is green. Grayscale: background region is dark, and target region is light.)
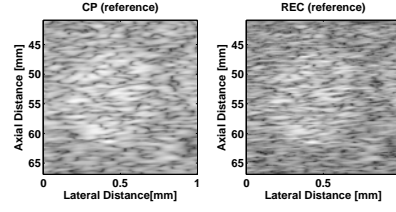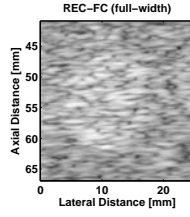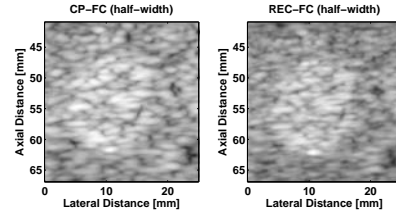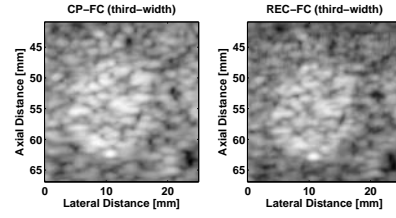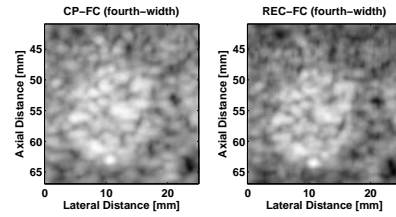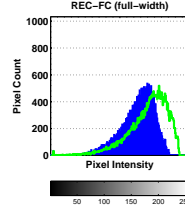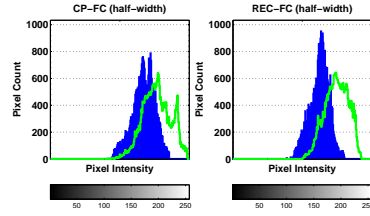
Figure 3.10: B-mode images of experimental measurements for the ATS +6 dB contrast target: (a) CP and REC reference scans, (b) REC-FC full width case, (c) CP-FC and REC-FC half-width cases, (d) CP-FC and REC-FC third-width cases, and (e) CP-FC and REC-FC fourth-width cases. Image dynamic range = -50 dB.
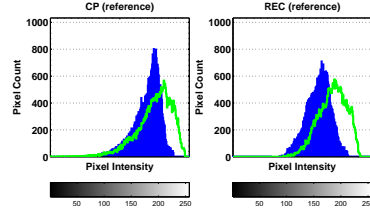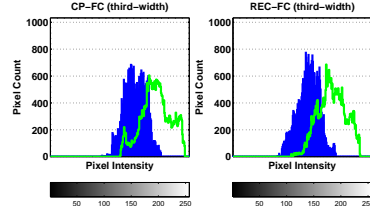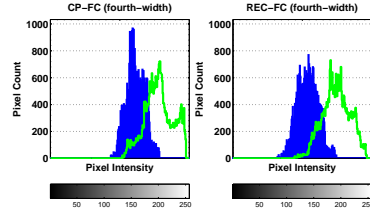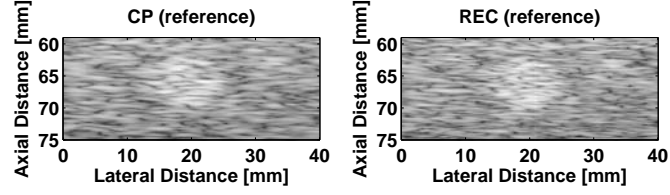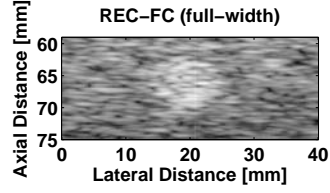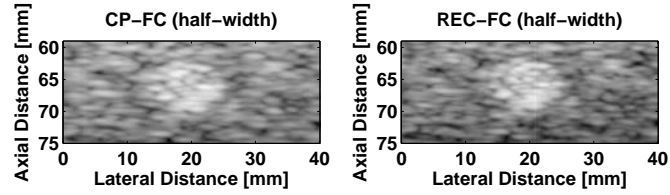
(a)

(b)

(c)

(d)

(e)

Figure 3.11: Histograms of experimental measurements for the ATS +6 dB contrast target: (a) CP and REC reference scans, (b) REC-FC full width case, (c) CP-FC and REC-FC half-width cases, (d) CP-FC and REC-FC third-width cases, and (e) CP-FC and REC-FC fourth-width cases. The pixel intensity is represented by the grayscale bar shown underneath the plot. (Color: background region is blue, and target region is green. Grayscale: background region is dark, and target region is light.)
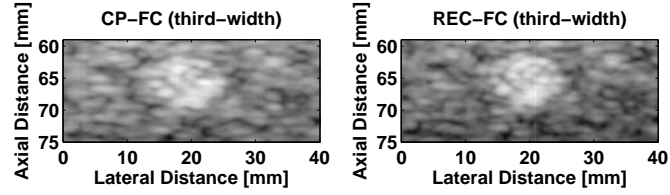
CP (reference)   REC (reference)

(a)

REC–FC (full–width)

(b)

CP–FC (half–width)   REC–FC (half–width)

(c)

CP–FC (third–width)   REC–FC (third–width)

(d)

CP–FC (fourth–width)   REC–FC (fourth–width)

(e)

Figure 3.12: B-mode images of experimental measurements of the hydrogel phantom for a lesion diameter of 8 mm: (a) CP and REC reference scans, (b) REC-FC full width case, (c) CP-FC and REC-FC half-width cases, (d) CP-FC and REC-FC third-width cases, and (e) CP-FC and REC-FC fourth-width cases. Image dynamic range = -50 dB.
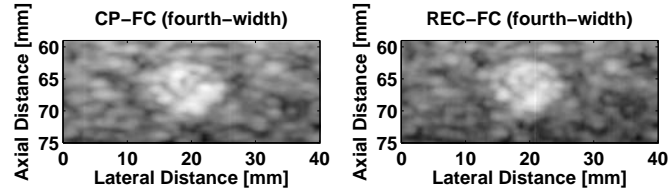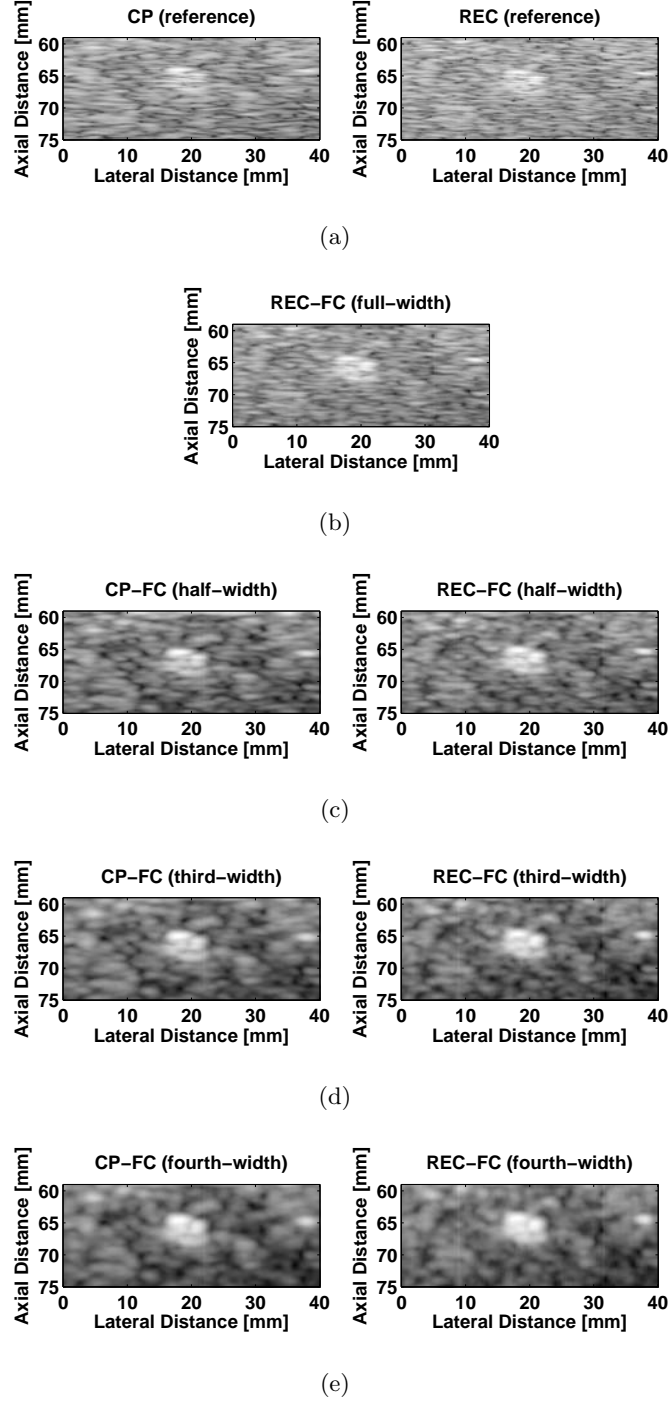
Figure 3.13: B-mode images of experimental measurements of the hydrogel phantom for a lesion diameter of 5 mm: (a) CP and REC reference scans, (b) REC-FC full width case, (c) CP-FC and REC-FC half-width cases, (d) CP-FC and REC-FC third-width cases, and (e) CP-FC and REC-FC fourth-width cases. Image dynamic range = -50 dB.

CP (reference)

REC (reference)

(a)

REC–FC (full–width)

(b)

CP–FC (half–width)

REC–FC (half–width)

(c)

CP–FC (third–width)

REC–FC (third–width)

(d)

CP–FC (fourth–width)

REC–FC (fourth–width)

(e)

Figure 3.14: B-mode images of experimental measurements of the hydrogel phantom for a lesion diameter of 3 mm: (a) CP and REC reference scans, (b) REC-FC full width case, (c) CP-FC and REC-FC half-width cases, (d) CP-FC and REC-FC third-width cases, and (e) CP-FC and REC-FC fourth-width cases. Image dynamic range = -50 dB.
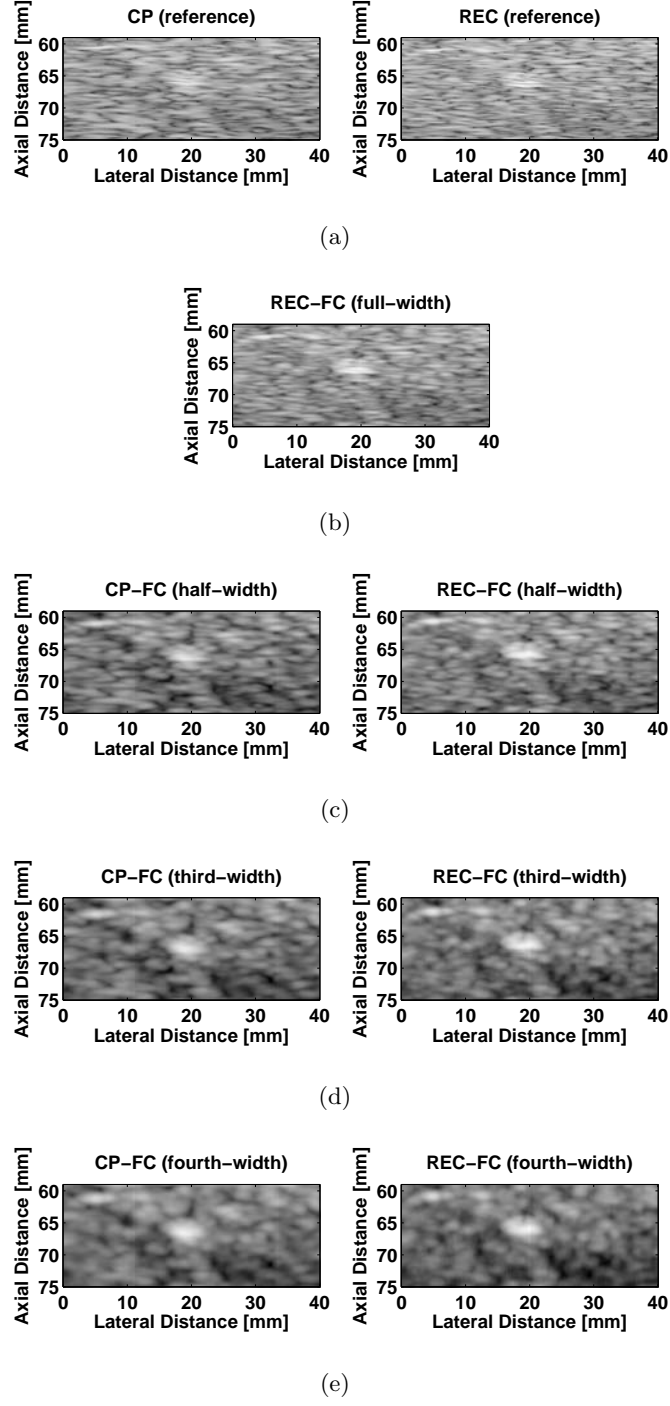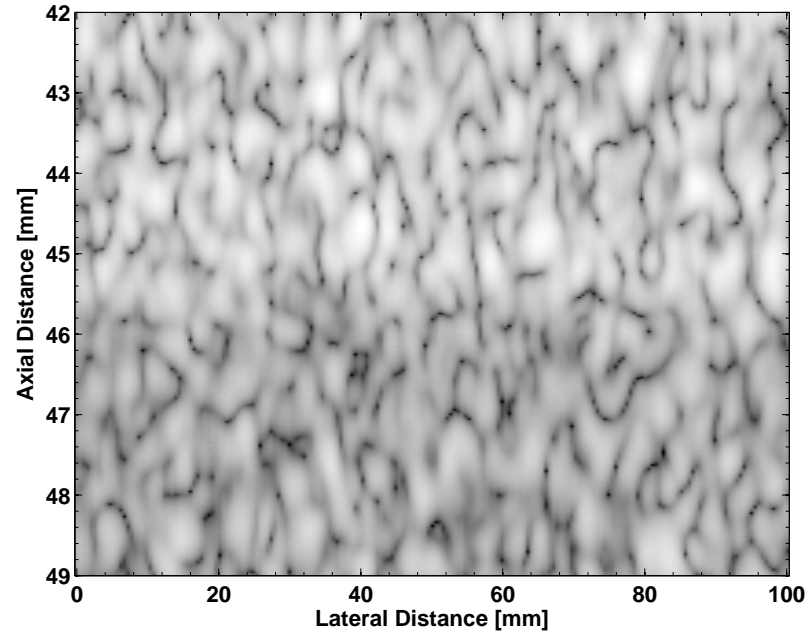
(a)
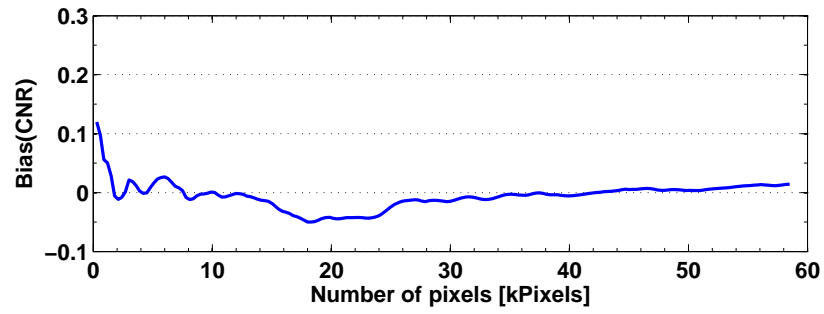
(b)

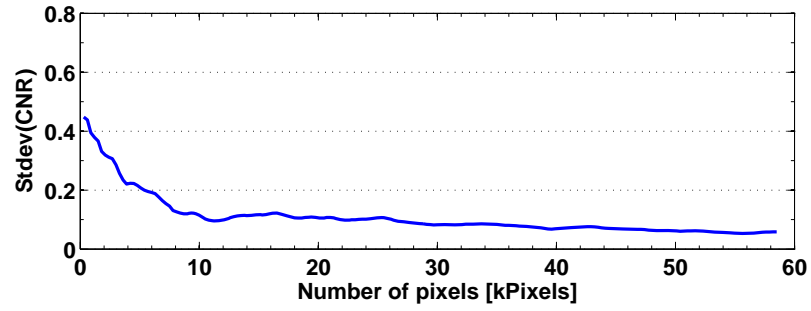Figure 3.15: (a) One of 25 phantoms used to evaluate CNR as a function of number of pixels. (b) Bias and standard deviation of CNR as function of number of pixels. Note that the bias was obtained by using the mean of the values in the range of 40 to 58 kilopixels.
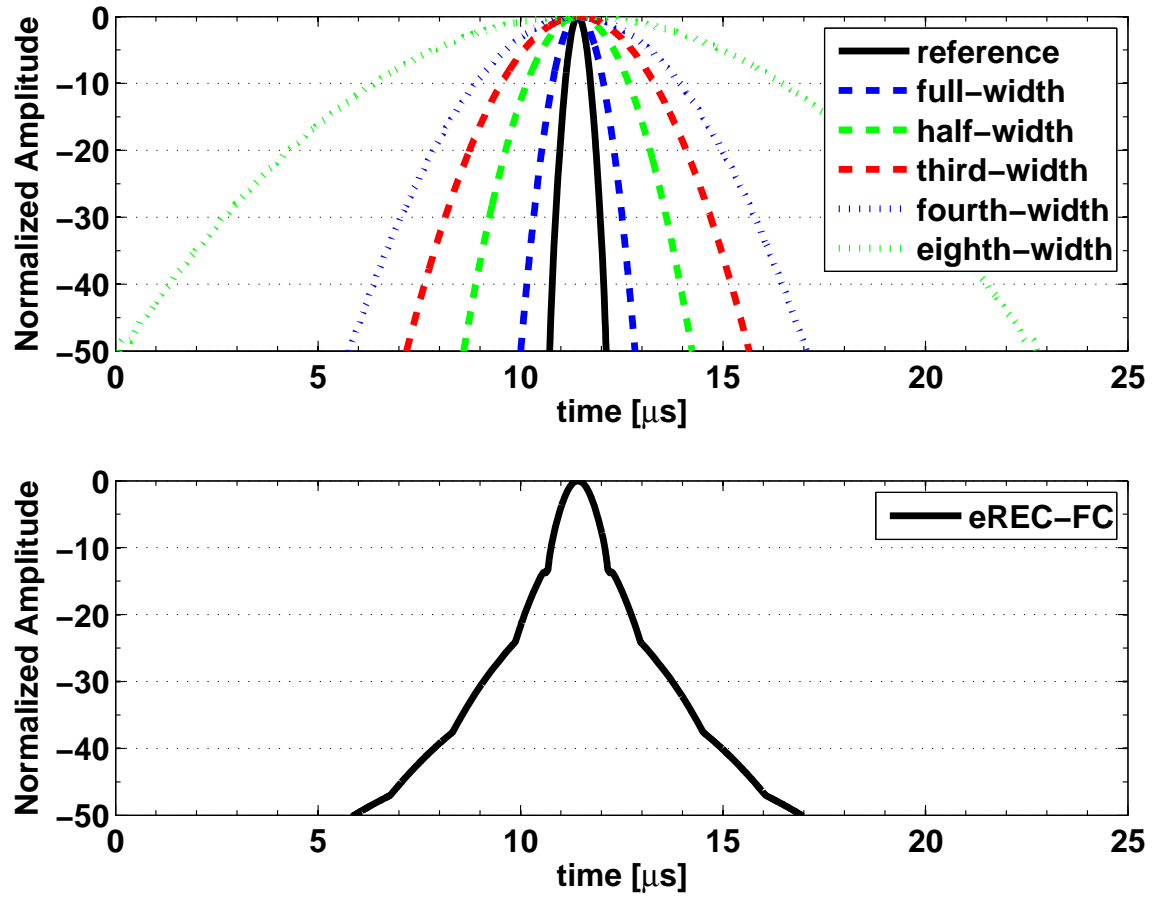
Figure 3.16: (a) Individual envelopes of the different frequency compounded images, and (b) resulting envelope from summing the individual envelopes.

Figure 3.17: B-mode images of experimental measurements of the ATS phantom for a contrast of +6 dB. The left panel represents the reference REC-FC image, the center panel represents the eREC-FC image, and the right panel corresponds to the REC-FC third-width case because it contains similar contrast. Image dynamic range = -50 dB.

Figure 3.18: B-mode images of experimental measurements of the ATS phantom for a contrast of +3 dB. The left panel represents the reference REC-FC image, the center panel represents the eREC-FC image, and the right panel corresponds to the REC-FC third-width case because it contains similar contrast. Image dynamic range = -50 dB.
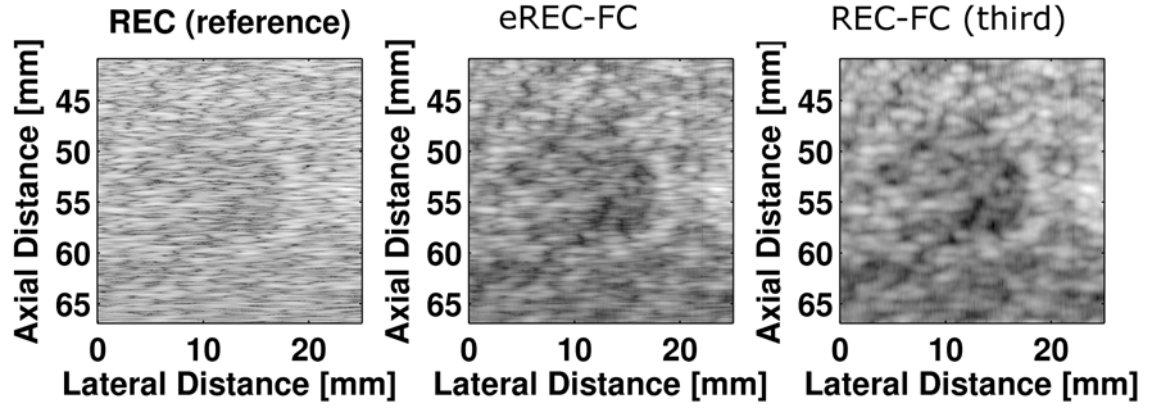
Figure 3.19: B-mode images of experimental measurements of the ATS phantom for a contrast of -3 dB. The left panel represents the reference REC-FC image, the center panel represents the eREC-FC image, and the right panel corresponds to the REC-FC third-width case because it contains similar contrast. Image dynamic range = -50 dB.
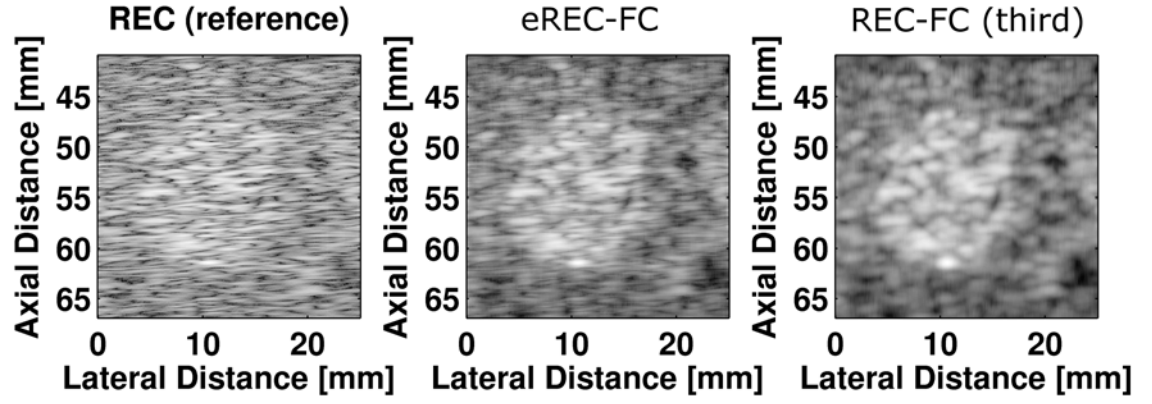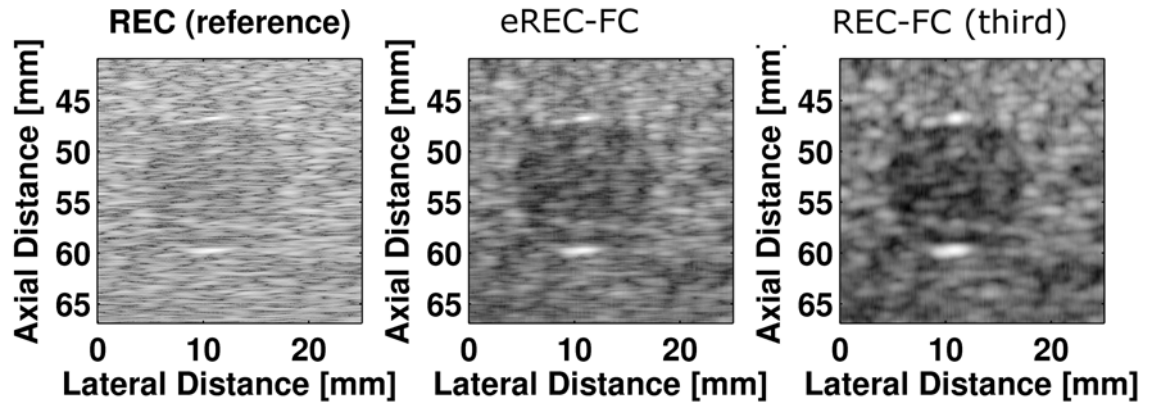
Figure 3.20: B-mode images of experimental measurements of the ATS phantom for a contrast of -6 dB. The left panel represents the reference REC-FC image, the center panel represents the eREC-FC image, and the right panel corresponds to the REC-FC third-width case because it contains similar contrast. Image dynamic range = -50 dB.
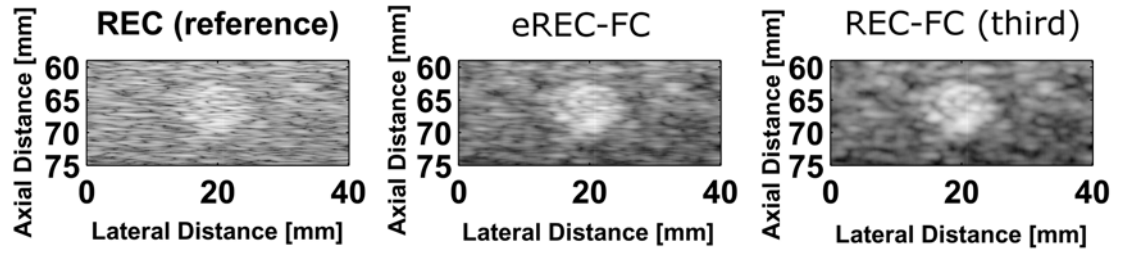
Figure 3.21: B-mode images of experimental measurements of the hydrogel cone phantom for a contrast of +6 dB and a lesion diameter of 8 mm. The left panel represents the reference REC-FC image, the center panel represents the eREC-FC image, and the right panel corresponds to the REC-FC third-width case because it contains similar contrast. Image dynamic range = -50 dB.
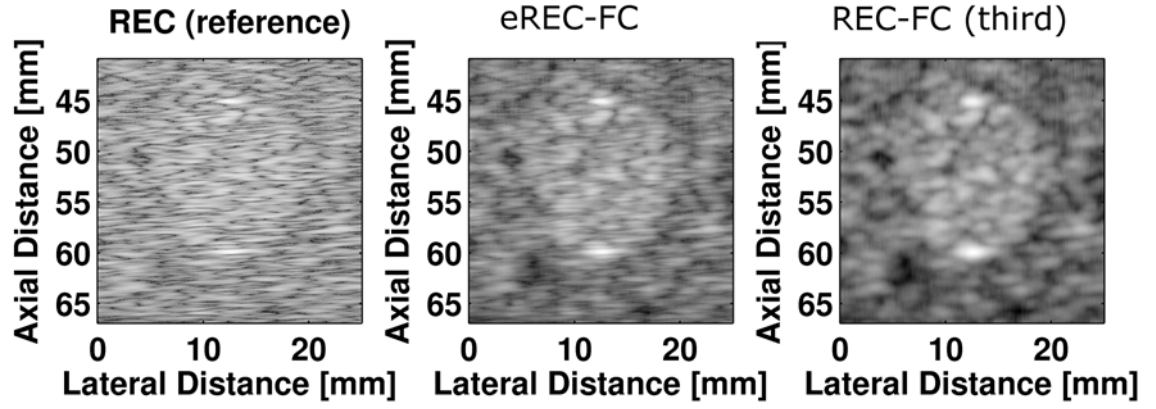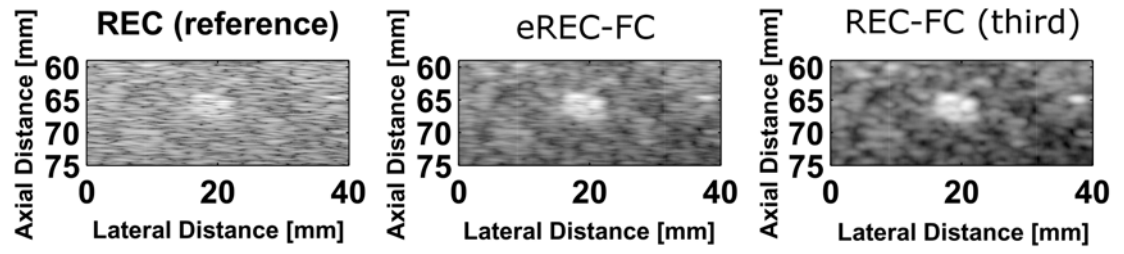
Figure 3.22: B-mode images of experimental measurements of the hydrogel cone phantom for a contrast of +6 dB and a lesion diameter of 5 mm. The left panel represents the reference REC-FC image, the center panel represents the eREC-FC image, and the right panel corresponds to the REC-FC third-width case because it contains similar contrast. Image dynamic range = -50 dB.
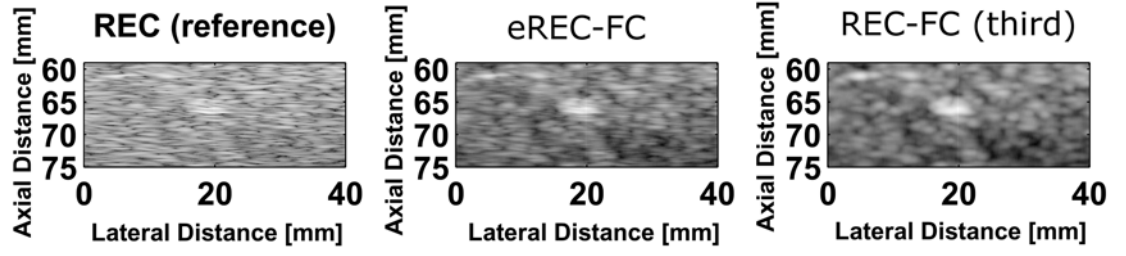
Figure 3.23: B-mode images of experimental measurements of the hydrogel cone phantom for a contrast of +6 dB and a lesion diameter of 3 mm. The left panel represents the reference REC-FC image, the center panel represents the eREC-FC image, and the right panel corresponds to the REC-FC third-width case because it contains similar contrast. Image dynamic range = -50 dB.
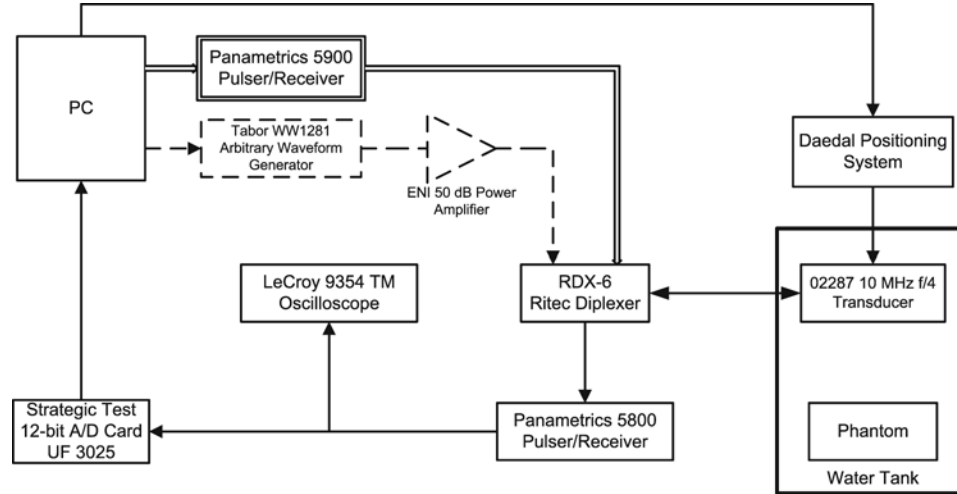
Figure 3.24: Experimental setup used for CP and REC. Note that solid lines indicate components used in both CP and REC experiments, while ⇒ indicates a path only taken during CP experiments whereas --→ indicates a path only taken during REC experiments.
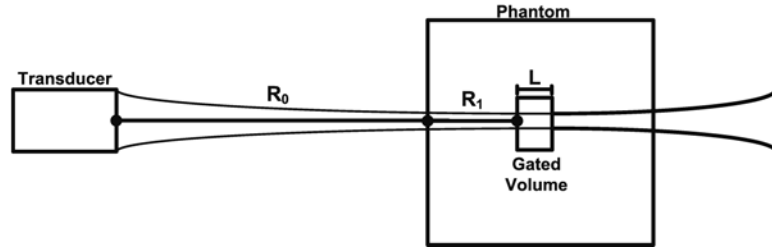
Figure 3.25: Distance relationship between the transducer and phantoms used to obtain measurements. R_0 is the distance from transducer surface to phantom surface, while R_1 is the distance from phantom surface to the start of the gated region of length L. The focal depth is at R0 + R1.
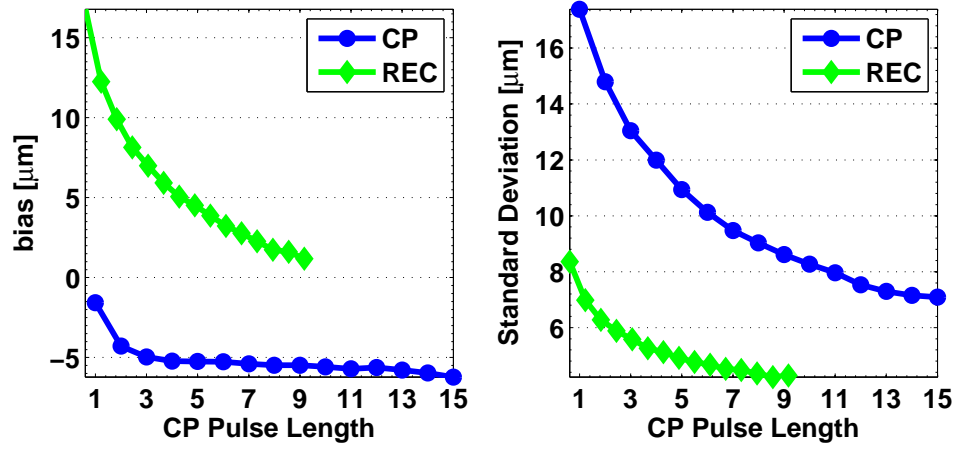
Figure 3.26: (a) Bias and (b) standard deviation of effective scatterer diameter estimates as a function of pulse length for 10 simulations of Phantom S1. Each tick mark on the abscissa is normalized to a CP pulse length of one (0.277 mm). Therefore, one REC pulse length (0.169 mm) would correspond to 0.610 CP pulse length.
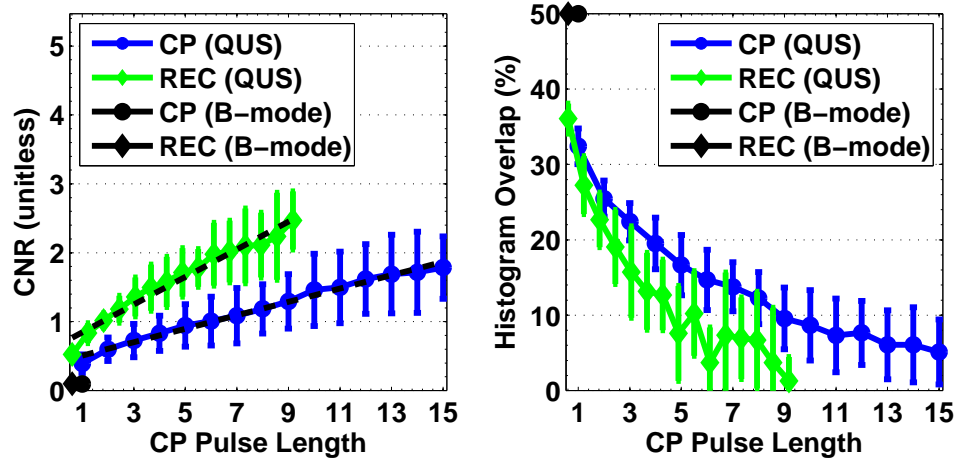
Figure 3.27: CNR and histogram overlap as a function of pulse length from 10 simulations of Phantom S2. Each tick mark on the abscissa is normalized to a CP pulse length of one (0.277 mm). Therefore, one REC pulse length (0.169 mm) would correspond to 0.610 CP pulse length.
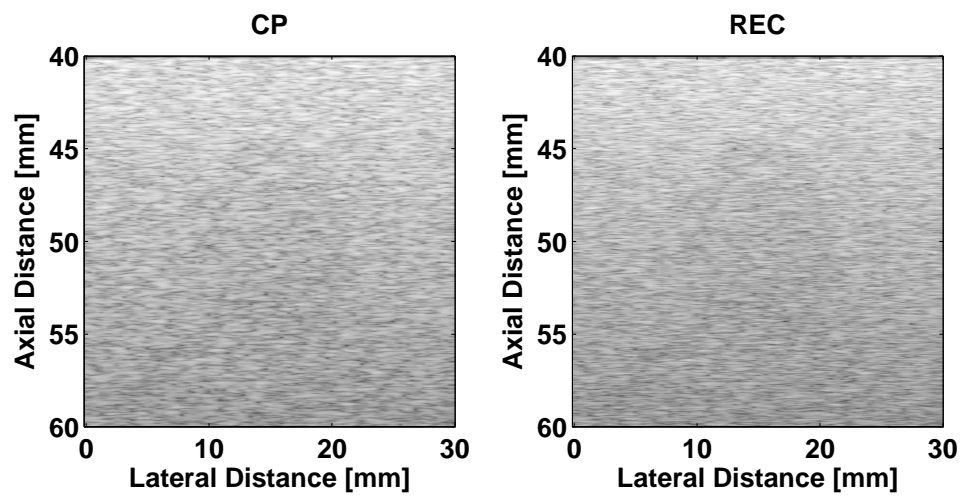
Figure 3.28: B-mode images of phantom S2 for CP and REC.

(a) 0.61 CP pulse lengths (b) 3.05 CP pulse lengths

(c) 6.10 CP pulse lengths (d) 9.15 CP pulse lengths
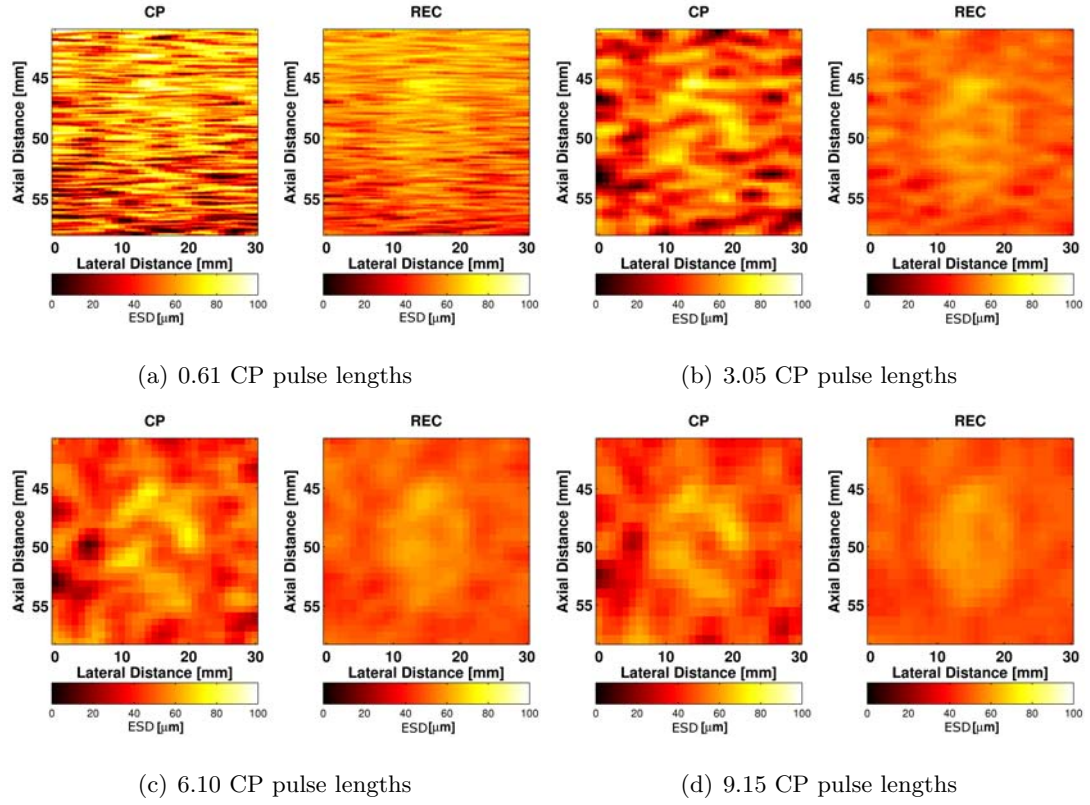
Figure 3.29: Parametric images of effective scatterer diameter for phantom S2 for CP and REC for various axial lengths. Actual scatterer diameters for lesion and background region were 60 μm and 50 μm, respectively.
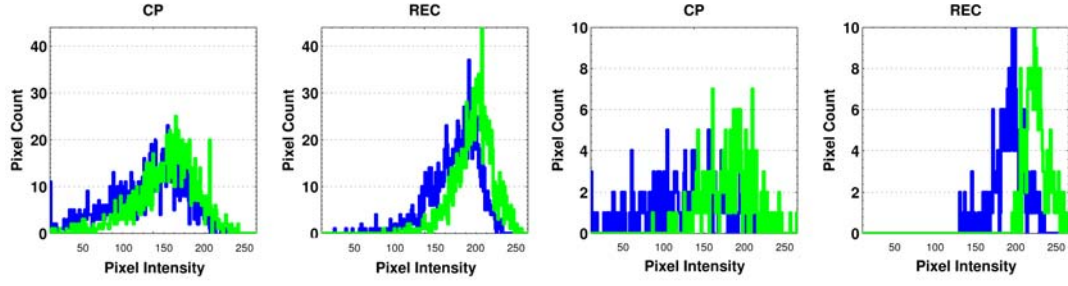
(a) 0.61 CP pulse lengths

(b) 3.05 CP pulse lengths
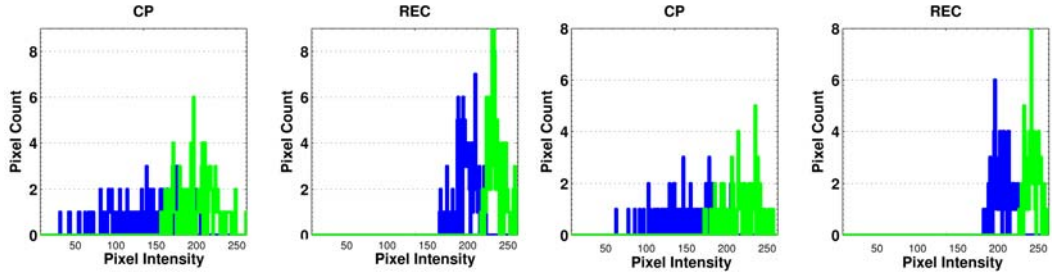
(c) 6.10 CP pulse lengths

(d) 9.15 CP pulse lengths

Figure 3.30: Histograms of pixel intensity for the background and target regions for phantom S2 for various axial lengths. The pixel intensity is represented by the grayscale colorbar shown underneath the plot. (Color: background region is blue, and target region is green. Grayscale: background region is dark, and target region is light.)
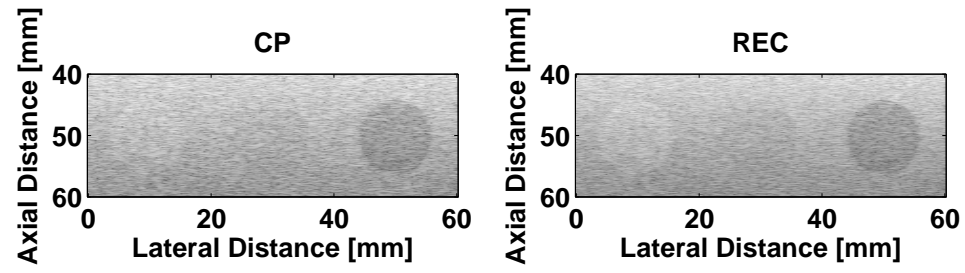
Figure 3.31: B-mode images of phantom S3 for CP and REC.
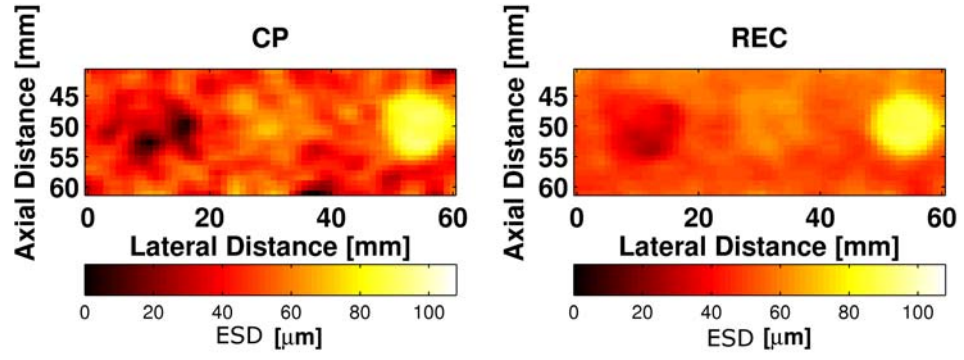
Figure 3.32: Parametric images of ESD for phantom S3 for CP and REC for the recommended axial length of 15 REC pulse lengths. Actual scatterer diameters for the three lesions (in order from left to right) and background region were 30 μm, 60 μm, 90 μm, and 50 μm, respectively.
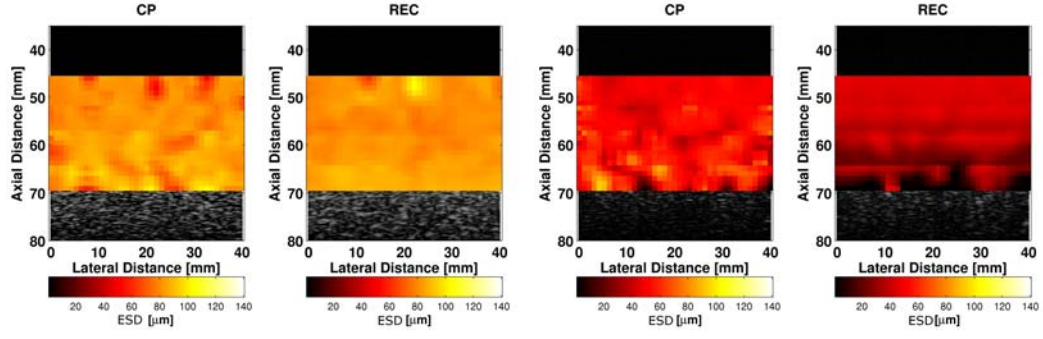
(a) Phantom A   (b) Phantom B
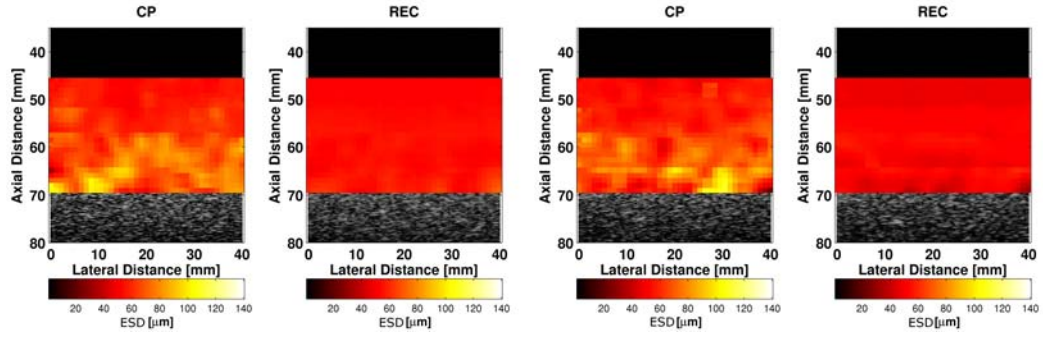
(c) Phantom C   (d) Phantom D

Figure 3.33: B-mode images for CP and REC with a parametric image overlay of ESD.
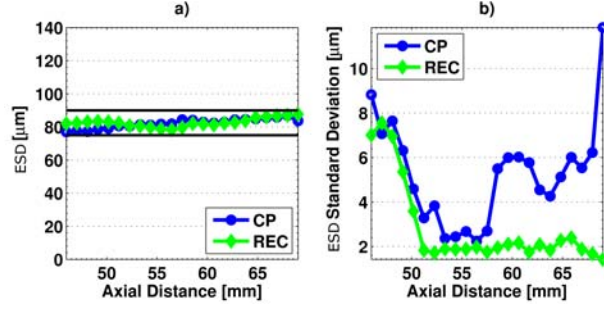
(a) Phantom A
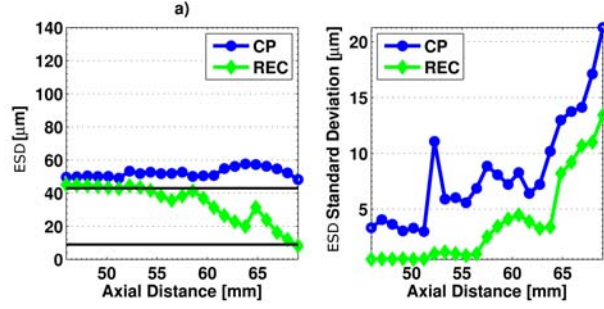
(b) Phantom B
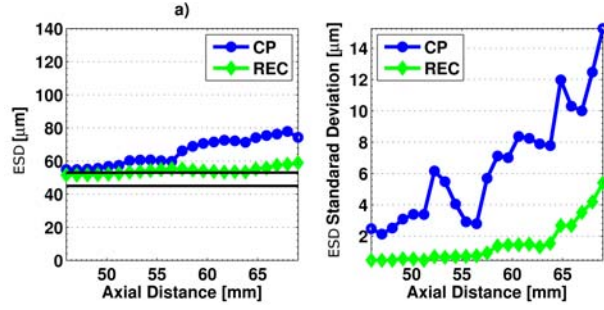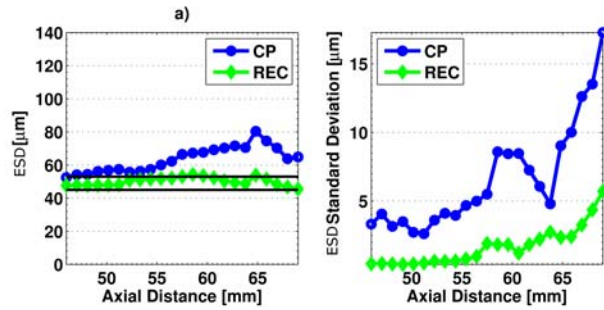
(c) Phantom C

(d) Phantom D

Figure 3.34: ESD and standard deviation of ESD estimates as a function of axial distance. The range of scatterers is indicated by solid lines across as a function of depth.
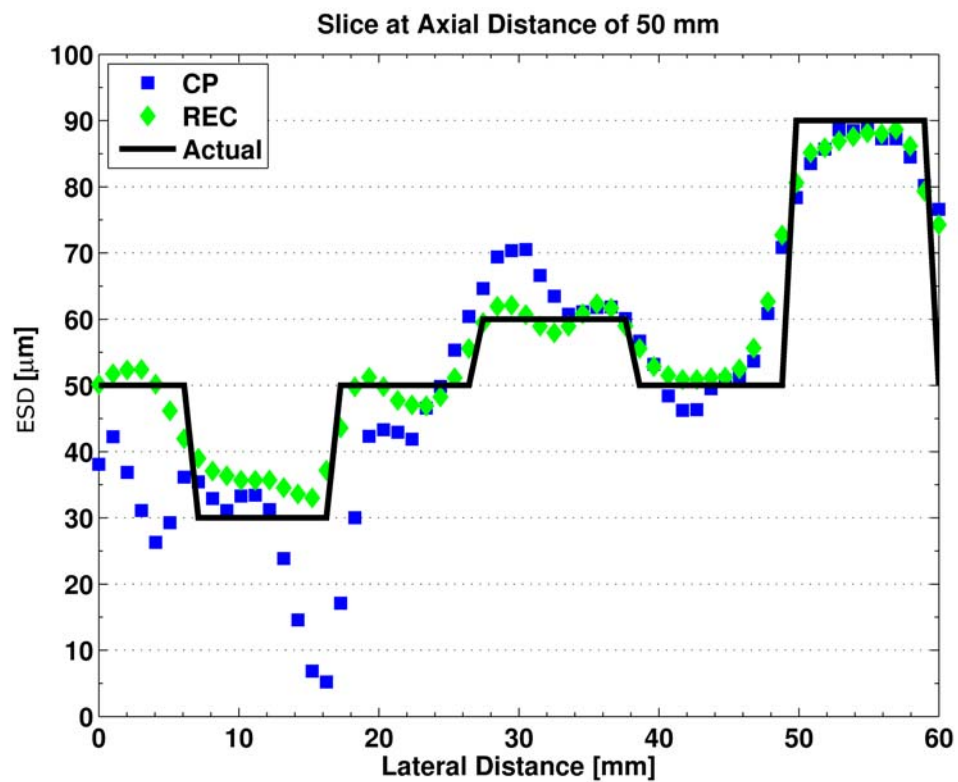
Figure 3.35: A lateral slice of the parametric image of Phantom S3 at an axial distance of 50 mm.

Table 3.1: Filter bank descriptions for the 50 cases of simulated RF data for a 15 mm target.

Technique[a]	Description[b]	Filter Banks		
		Bandwidth (MHz)	Separation (MHz)	Quantity
CP	reference scan	1.1	–	0
REC	reference scan	2.2	–	0
REC-FC	full width of CP BW	1.1	1.3	3
CP-FC	1/2 width of CP BW	0.6	0.6	4
REC-FC	1/2 width of CP BW	0.6	0.6	7
CP-FC	1/3 width of CP BW	0.4	0.4	6
REC-FC	1/3 width of CP BW	0.4	0.4	10
CP-FC	1/4 width of CP BW	0.3	0.3	8
REC-FC	1/4 width of CP BW	0.3	0.3	13

[a] CP = conventional pulsing, REC = resolution enhancement compression, FC = frequency compounding
[b] BW = bandwidth

Table 3.2: Axial and lateral correlation length for the 50 cases of simulated RF data for a 15 mm target.

Technique[a]	Description[b]	Resolution[c]	
		Axial	Lateral
		(mm)	(mm)
CP	reference scan	0.30 ± 0.03	1.27 ± 0.44
REC	reference scan	0.20 ± 0.01	1.37 ± 0.49
		(33%)	(8%)
REC-FC	full width of CP BW	0.44 ± 0.05	1.70 ± 0.57
		(47%)	(34%)
CP-FC	1/2 width of CP BW	0.82 ± 0.13	1.66 ± 0.65
		(169%)	(31%)
REC-FC	1/2 width of CP BW	0.89 ± 0.16	1.78 ± 0.54
		(194%)	(40%)
CP-FC	1/3 width of CP BW	1.17 ± 0.23	1.70 ± 0.49
		(285%)	(34%)
REC-FC	1/3 width of CP BW	1.37 ± 0.32	1.76 ± 0.50
		(351%)	(39%)
CP-FC	1/4 width of CP BW	1.48 ± 0.29	1.70 ± 0.53
		(386%)	(34%)
REC-FC	1/4 width of CP BW	1.77 ± 0.39	1.74 ± 0.51
		(485%)	(37%)

[a] CP = conventional pulsing, REC = resolution enhancement compression, FC = frequency compounding

[b] BW = bandwidth

[c] The resolution values in the table are described in terms of the mean plus/minus one standard deviation. Values in parentheses represent the absolute percent change of REC-FC vs. CP reference.

Table 3.3: CNR and sSNR for the 50 cases of simulated RF data for a 15 mm target.

Technique[a]	Description[b]	CNR[c]	sSNR$_B$[c]	sSNR$_T$[c]
CP	reference scan	0.74 ± 0.14	1.94 ± 0.11	1.90 ± 0.11
REC	reference scan	0.74 ± 0.10	1.94 ± 0.10	1.89 ± 0.08
		(0%)	(0%)	(0%)
REC	full width of CP BW	1.27 ± 0.17	2.98 ± 0.24	2.87 ± 0.19
		(71%)	(53%)	(51%)
CP	1/2 width of CP BW	1.41 ± 0.26	3.22 ± 0.33	3.05 ± 0.27
		(89%)	(65%)	(60%)
REC	1/2 width of CP BW	1.77 ± 0.23	3.97 ± 0.36	3.71 ± 0.32
		(137%-25%)	(103%-23%)	(95%-22%)
CP	1/3 width of CP BW	1.73 ± 0.31	3.88 ± 0.49	3.44 ± 0.35
		(133%)	(99%)	(81%)
REC	1/3 width of CP BW	2.14 ± 0.30	4.77 ± 0.60	4.08 ± 0.38
		(187%-24%)	(144%-23%)	(114%-18%)
CP	1/4 width of CP BW	2.01 ± 0.38	4.47 ± 0.64	3.49 ± 0.35
		(170%)	(129%)	(83%)
REC	1/4 width of CP BW	2.46 ± 0.37	5.49 ± 0.77	4.00 ± 0.40
		(231%-22%)	(181%-23%)	(110%-15%))

[a] CP = conventional pulsing, REC = resolution enhancement compression, FC = frequency compounding

[b] BW = bandwidth

[c] The values are described in terms of the mean plus/minus one standard deviation. In parentheses: the absolute percent change of REC-FC vs. CP reference - absolute percent change of REC-FC vs. CP-FC for the same case.

Table 3.4: HPI, HO and lSNR for the 50 cases of simulated RF data for a 15 mm target.

Technique[a]	Description[b]	HPI$_B$[c]	HPI$_T$[c]	HO	lSNR[c]
CP	reference scan	169.3 ± 28.1	199.0 ± 28.6	28	15.86 ± 2.80
REC	reference scan	165.3 ± 27.9 (2%)	194.9 ± 28.4 (2%)	28	18.21 ± 3.00 (15%)
REC	full width of CP BW	181.5 ± 16.3 (7%)	211.3 ± 16.7 (6%)	18	18.77 ± 3.62 (18%)
CP	1/2 width of CP BW	187.6 ± 14.9 (11%)	217.7 ± 15.3 (9%)	16	15.85 ± 3.32 (0%)
REC	1/2 width of CP BW	192.1 ± 11.8 (13%-2%)	222.1 ± 12.1 (12%-2%)	10	18.29 ± 3.51 (15%-15%)
CP	1/3 width of CP BW	194.4 ± 12.1 (15%)	224.5 ± 12.6 (13%)	11	15.55 ± 3.06 (2%)
REC	1/3 width of CP BW	196.8 ± 10.0 (16%-1%)	227.6 ± 10.3 (14%-1%)	6	17.33 ± 3.37 (9%-11%)
CP	1/4 width of CP BW	198.8 ± 10.4 (17%)	228.9 ± 10.8 (15%)	8	14.60 ± 3.22 (8%)
REC	1/4 width of CP BW	198.8 ± 10.4 (17%-0%)	229.0 ± 18.8 (15%-0%)	4	15.52 ± 3.16 (2%-6%)

[a] CP = conventional pulsing, REC = resolution enhancement compression, FC = frequency compounding
[b] BW = bandwidth
[c] The values are described in terms of the mean plus/minus one standard deviation. In parentheses: absolute percent change of REC-FC vs. CP reference - absolute percent change of REC-FC vs. CP-FC for the same case.

Table 3.5: Filter bank descriptions for the experimental results for the +6 dB, 15 mm diameter target from the ATS phantom and the hydrogel cone phantom.

| | | Filter Banks | | |
| | | Bandwidth | Separation | |
Technique[a]	Description[b]	(MHz)	(MHz)	Quantity
CP	reference scan	1.2	–	0
REC	reference scan	2.4	–	0
REC-FC	full width of CP BW	1.2	1.1	4
CP-FC	1/2 width of CP BW	0.6	0.6	3
REC-FC	1/2 width of CP BW	0.6	0.6	6
CP-FC	1/3 width of CP BW	0.4	0.4	6
REC-FC	1/3 width of CP BW	0.4	0.4	10
CP-FC	1/4 width of CP BW	0.3	0.3	10
REC-FC	1/4 width of CP BW	0.3	0.3	15

[a] CP = conventional pulsing, REC = resolution enhancement compression, FC = frequency compounding
[b] BW = bandwidth

Table 3.6: Axial and lateral correlation length for the experimental results for the +6 dB, 15 mm diameter target from the ATS phantom.

Technique[a]	Description[b]	Resolution[c]	
		Axial	Lateral
		(mm)	(mm)
CP	reference scan	0.39	1.2
REC	reference scan	0.21	1.2
		(46%)	(0%)
REC-FC	full width of CP BW	0.37	1.2
		(5%)	(0%)
CP-FC	1/2 width of CP BW	0.68	1.2
		(74%)	(0%)
REC-FC	1/2 width of CP BW	0.45	1.0
		(15%)	(16%)
CP-FC	1/3 width of CP BW	0.80	1.2
		(105%)	(0%)
REC-FC	1/3 width of CP BW	0.65	1.4
		(67%)	(16%)
CP-FC	1/4 width of CP BW	1.25	1.2
		(221%)	(0%)
REC-FC	1/4 width of CP BW	1.34	1.2
		(244%)	(0%)

[a] CP = conventional pulsing, REC = resolution enhancement compression, FC = frequency compounding

[b] BW = bandwidth

[c] Values in parentheses represent the absolute percent change of REC-FC vs. CP reference.

Table 3.7: CNR, and sSNR for the experimental results for the +6 dB, 15 mm diameter target from the ATS phantom.

Technique[a]	Description[b]	CNR[c]	sSNR$_B$[c]	sSNR$_T$[c]
CP	reference scan	0.33	2.09	1.71
REC	reference scan	0.42	1.93	1.84
		(25%)	(7%)	(8%)
REC	full width of CP BW	0.74	2.95	2.68
		(121%)	(41%)	(57%))
CP	1/2 width of CP BW	0.71	2.99	2.34
		(112%)	(43%)	(37%)
REC	1/2 width of CP BW	1.11	4.13	3.49
		(231%-56%)	(98%-38%)	(104%-49%)
CP	1/3 width of CP BW	1.11	4.24	3.08
		(233%)	(102%)	(80%)
REC	1/3 width of CP BW	1.35	5.27	4.20
		(302%-21%)	(152%-24%)	(146%-36%)
CP	1/4 width of CP BW	1.37	5.36	3.56
		(309%)	(156%)	(108%)
REC	1/4 width of CP BW	1.65	6.03	4.84
		(391%-20%)	(189%-13%)	(183%-36%)

[a] CP = conventional pulsing, REC = resolution enhancement compression, FC = frequency compounding

[b] BW = bandwidth

[c] Values in parentheses represent the absolute percent change of REC-FC vs. CP reference.

Table 3.8: HPI, HO and lSNR for the experimental results for the +6 dB, 15 mm diameter target from the ATS phantom.

Technique[a]	Description[b]	HPI_B[c]	HPI_T[c]	HO	lSNR[c]
CP	reference scan	180.0 ± 26.4	193.8 ± 31.5	35	9.9
REC	reference scan	176.8 ± 27.1	193.5 ± 29.6	35	14.6
		(2%)	(0%)		(48%)
REC	full width of CP BW	158.0 ± 22.5	183.1 ± 25.4	33	17.6
		(12%)	(6%)		(78%)
CP	1/2 width of CP BW	174.9 ± 20.0	197.4 ± 24.5	33	15.0
		(3%)	(2%)		(52%)
REC	1/2 width of CP BW	159.8 ± 18.1	190.8 ± 21.3	28	26.1
		(11%-9%)	(2%-3%)		(164%-74%)
CP	1/3 width of CP BW	161.3 ± 18.8	197.0 ± 25.7	28	17.8
		(10%)	(2%)		(80%)
REC	1/3 width of CP BW	139.3 ± 20.0	182.4 ± 25.0	21	23.6
		(23%-14%)	(6%-7%)		(139%-33%)
CP	1/4 width of CP BW	157.6 ± 16.9	199.5 ± 25.5	25	17.5
		(12%)	(3%)		(78%)
REC	1/4 width of CP BW	138.5 ± 19.6	190.4 ± 24.8	19	22.7
		(23%-12%)	(2%-5%)		(130%-30%)

[a] CP = conventional pulsing, REC = resolution enhancement compression, FC = frequency compounding

[b] BW = bandwidth

[c] Values in parentheses represent the absolute percent change of REC-FC vs. CP reference.

Table 3.9: CNR experimental results for the +6 dB hydrogel phantom at various diameters.

		Lesion Diameter[c]		
Technique[a]	Description[b]	8 mm	5 mm	3 mm
CP	reference scan	0.82	1.22	1.40
REC	reference scan	0.95	1.23	1.66
		(16%)	(1%)	(19%)
REC	full width of CP BW	1.53	2.50	3.65
		(87%)	(105%)	(161%)
CP	1/2 width of CP BW	1.68	4.09	4.24
		(104%)	(235%)	(202%)
REC	1/2 width of CP BW	2.14	4.40	2.42
		(161%-27%)	(261%-8%)	(73%-42%)
CP	1/3 width of CP BW	1.99	3.90	3.56
		(142%)	(219%)	(154%)
REC	1/3 width of CP BW	2.58	5.56	5.41
		(283%-30%)	(355%-43%)	(301%-52%)
CP	1/4 width of CP BW	2.01	4.34	7.44
		(145%)	(255%)	(431%)
REC	1/4 width of CP BW	3.00	7.22	5.00
		(265%-50%)	(491%-66%)	(257%-48%)

[a] CP = conventional pulsing, REC = resolution enhancement compression, FC = frequency compounding

[b] BW = bandwidth

[c] In parentheses: absolute percent change of REC-FC vs. CP reference - absolute percent change of REC-FC vs. CP-FC for the same case.

Table 3.10: $sSNR_B$ experimental results for the +6 dB hydrogel phantom at various diameters.

		Lesion Diameter[c]		
Technique[a]	Description[b]	8 mm	5 mm	3 mm
CP	reference scan	1.56	1.79	2.01
REC	reference scan	1.66	2.31	2.06
		(6%)	(29%)	(3%)
REC	full width of CP BW	2.33	2.87	3.47
		(49%)	(60%)	(72%)
CP	1/2 width of CP BW	2.08	3.51	2.38
		(33%)	(96%)	(18%)
REC	1/2 width of CP BW	2.81	4.46	3.04
		(80%-27%)	(149%-27%)	(51%-27%)
CP	1/3 width of CP BW	2.78	5.73	2.85
		(78%)	(220%)	(41%)
REC	1/3 width of CP BW	3.81	2.07	4.82
		(144%-37%)	(15%-33%)	(139%-69%)
CP	1/4 width of CP BW	2.65	3.87	6.88
		(70%)	(48%)	(242%)
REC	1/4 width of CP BW	4.35	1.98	7.48
		(179%-64%)	(11%-48%)	(272%-8%)

[a] CP = conventional pulsing, REC = resolution enhancement compression, FC = frequency compounding

[b] BW = bandwidth

[c] In parentheses: absolute percent change of REC-FC vs. CP reference - absolute percent change of REC-FC vs. CP-FC for the same case.

Table 3.11: sSNR$_T$ experimental results for the +6 dB hydrogel phantom at various diameters.

		Lesion Diameter[c]		
Technique[a]	Description[b]	8 mm	5 mm	3 mm
CP	reference scan	2.10	2.05	2.36
REC	reference scan	2.16	2.86	1.77
		(3%)	(40%)	(25%)
REC	full width of CP BW	3.17	4.26	6.41
		(51%)	(108%)	(172%)
CP	1/2 width of CP BW	3.99	3.26	9.23
		(90%)	(59%)	(291%)
REC	1/2 width of CP BW	5.25	4.22	6.25
		(150%-17%)	(106%-1%)	(165%-32%)
CP	1/3 width of CP BW	4.50	4.28	3.33
		(114%)	(108%)	(41%)
REC	1/3 width of CP BW	6.71	3.99	7.79
		(220%-49%)	(95%-7%)	(230%-134%)
CP	1/4 width of CP BW	4.43	4.64	5.33
		(110%)	(126%)	(126%)
REC	1/4 width of CP BW	8.51	2.42	4.77
		(305%-92%)	(18%-47%)	(102%-11%)

[a] CP = conventional pulsing, REC = resolution enhancement compression, FC = frequency compounding

[b] BW = bandwidth

[c] In parentheses: absolute percent change of REC-FC vs. CP reference - absolute percent change of REC-FC vs. CP-FC for the same case.

Table 3.12: CNR results for the eREC-FC B-mode images and for the REC reference B-mode images.

Phantom Description	CNR	
	REC (reference)	eREC-FC
ATS +6 dB	0.42	1.01
ATS +3 dB	0.46	1.04
ATS -3 dB	0.74	1.36
ATS -6 dB	0.44	1.24
Hydrogel 8 mm	0.95	2.40
Hydrogel 5 mm	1.23	3.03
Hydrogel 3 mm	1.66	3.27

Table 3.13: Simulated Phantom (S1 and S2) properties.

Property	Phantom		
	S1	S2	
		lesion	background
Phantom Dimensions - length, width, height (mm)	20 x 30 x 1.2	20 x 30 x 1.2	
Scatterer Type	Gaussian	Gaussian	Gaussian
Scatterer Diameter (μm)	50	60	50
Lesion Diameter (mm)	-	12	-
Nominal sound speed (m/s)	1540	1540	1540
Nominal Attenuation (dB/(MHz cm))	0.5	0.5	0.5
CP: ka (10 MHz @ -6 dB)	0.61 - 1.42	0.73 - 1.71	0.61 - 1.42
REC: ka (10 MHz @ -6 dB)	0.26 - 1.79	0.30 - 2.14	0.26 - 1.79

Table 3.14: Simulated Phantoms (S3) properties.

| Property | Phantom | | | |
| | S3 | | | |
	lesion 1	lesion 2	lesion 3	background
Phantom Dimensions - l,w,h (mm)	20 x 30 x 1.2			
Scatterer Type	Gaussian	Gaussian	Gaussian	Gaussian
Scatterer Diameter (μm)	30	60	90	-
Lesion Diameter (mm)	12	12	12	-
Nominal sound speed (m/s)	1540	1540	1540	1540
Nominal Attenuation (dB/(MHz cm))	0.5	0.5	0.5	0.5
CP: ka (10 MHz @ -6 dB)	0.37 - 0.85	0.73 - 1.71	1.46 - 3.42	
REC: ka (10 MHz @ -6 dB)	0.15 - 1.07	0.30 - 2.14	0.60 - 4.28	

Table 3.15: Experimental Phantom properties: Part I.

Property	Phantom	
	A	B
Scatterer	Glass spheres	Glass spheres
Materials	Agarose/n-propanol/	Agarose/n-propanol
	milk/$H_2$0	milk/$H_2$0
Scatterer diameter (μm)	75 - 90	9 - 43
Nominal sound speed (m/s)	1540	1540
Nominal Attenuation (dB/(MHz cm))	0.5	0.7
CP: ka (10 MHz @ -6 dB)	1.70 - 4.37	0.20 - 2.19
REC: ka (10 MHz @ -6 dB)	0.97 - 6.04	0.12 - 3.02

Table 3.16: Experimental Phantom properties: Part II.

	Phantom	
Property	C	D
Scatterer	Glass spheres	Glass spheres
Materials	Agarose/n-propanol/	Agarose/n-propanol/
	graphite/$H_2$0	graphite/$H_2$0
Scatterer diameter (μm)	45 - 53	45 - 53
Nominal sound speed (m/s)	1540	1540
Nominal Attenuation (dB/(MHz cm))	0.5	0.7
CP: ka (10 MHz @ -6 dB)	1.02 - 2.58	1.02 - 2.58
REC: ka (10 MHz @ -6 dB)	0.58 - 3.56	0.58 - 3.56

Table 3.17: Bias $\pm$ one standard deviation results for QUS images of 10 S2 phantoms using ROIs with different axial sizes in terms of CP pulse lengths.

CP Pulse Lengths	bias			
	μm			
	CP		REC	
	lesion	background	lesion	background
0.61	-0.10 $\pm$ 15.59	2.46 $\pm$ 18.30	7.69 $\pm$ 5.85	17.69 $\pm$ 6.60
3.05	-2.23 $\pm$ 9.69	-3.78 $\pm$ 12.97	-2.11 $\pm$ 3.35	7.88 $\pm$ 4.08
6.10	-2.07 $\pm$ 6.78	-3.85 $\pm$ 9.52	-5.44 $\pm$ 2.56	4.55 $\pm$ 3.17
9.15	-2.01 $\pm$ 5.41	-3.77 $\pm$ 6.89	-7.28 $\pm$ 2.08	2.71 $\pm$ 2.66

Table 3.18: Histogram overlap, and CNR $\pm$ one standard deviation results for QUS images of 10 S2 phantoms uisng ROIs with different axial sizes in terms of CP pulse lengths.

CP Pulse Lengths	histogram overlap		CNR	
	%		unitless	
	CP	REC	CP	REC
	lesion	background	lesion	background
0.61	36.70 ± 1.36	36.08 ± 1.99	0.31 ± 0.09	0.52 ± 0.07
3.05	21.70 ± 3.29	15.72 ± 6.08	0.72 ± 0.23	1.36 ± 0.28
6.10	13.75 ± 4.30	3.71 ± 4.66	1.02 ± 0.36	1.98 ± 0.45
9.15	9.14 ± 4.28	1.27 ± 3.18	1.36 ± 0.46	2.47 ± 0.42

Table 3.19: CNR and standard deviation results for Phantoms S3 at a recommended axial length of 15 REC pulse length.

	CNR		ESD Standard Deviation	
	unitless		μm	
Scatterer Diameter	CP	REC	CP	REC
30	2.28	3.31	8.56	4.04
60	1.45	3.66	4.78	1.51
90	6.67	16.80	1.71	1.05

Table 3.20: Experimental results of out of range, ESD, and standard deviation of ESD estimates for all depths (axial distance) combined for the physical phantoms.

phantom	Out of range %		ESD μm		Standard deviation(ESD) μm	
	CP	REC	CP	REC	CP	REC
A	17.9	4.4	83.0	82.6	6.4	4.2
B	87.2	37.9	52.4	33.8	9.6	10.9
C	93.4	61.3	65.6	54.1	10.8	2.7
D	87.2	20.5	63.6	50.1	10.9	3.2